nature protocols

PROTOCOL

https://doi.org/10.1038/s41596-020-00457-2

Check for updates

Mapping mechanical properties of biological materials via an add-on Brillouin module to confocal microscopes

Jitao Zhang[1,2]✉ and Giuliano Scarcelli[1,2]✉

Several techniques have been developed over the past few decades to assess the mechanical properties of biological samples, which has fueled a rapid growth in the fields of biophysics, bioengineering, and mechanobiology. In this context, Brillouin optical spectroscopy has long been known as an intriguing modality for noncontact material characterization. However, limited by speed and sample damage, it had not translated into a viable imaging modality for biomedically relevant materials. Recently, based on a novel spectroscopy strategy that substantially improves the speed of Brillouin measurement, confocal Brillouin microscopy has emerged as a unique complementary tool to traditional methods as it allows noncontact, nonperturbative, label-free measurements of material mechanical properties. The feasibility and potential of this innovative technique at both the cell and tissue level have been extensively demonstrated over the past decade. As Brillouin technology is rapidly recognized, a standard approach for building and operating Brillouin microscopes is required to facilitate the widespread adoption of this technology. In this protocol, we aim to establish a robust approach for instrumentation, and data acquisition and analysis. By carefully following this protocol, we expect that a Brillouin instrument can be built in 5–9 days by a person with basic optics knowledge and alignment experience; the data acquisition as well as postprocessing can be accomplished within 2–8 h.

Introduction

Biomechanical interactions are recognized as a central player in the regulation of cellular functions (e.g., proliferation, migration, and gene expression)[1,2] as well as system-level behaviors (tissue morphogenesis, cancer metastasis, and angiogenesis)[3–5]. To characterize the mechanical interplay within biological samples, such as cells, tissue, and biomaterials, tools to identify mechanically related pathways[6], measure deformations and forces[7], and quantify material mechanical properties are required[8,9]. Assessing material mechanical properties has been greatly advanced by the development of many important techniques, which can be loosely classified into three categories: (i) Contact-based techniques, where a stress is applied to the sample and the corresponding strain is quantified to extract the modulus. These include indentation methods such as atomic force microscopy (AFM)[10–14] and other cantilever-based tools[15,16], micropipette aspiration[17,18], parallel-plate rheometry[19], and stretching substrate[20]. (ii) Bead-based techniques, where external beads are attached to or injected into the sample and their behavior is monitored to extract material properties. These include optical tweezer[21,22], magnetic twisting cytometry (MTC)[23,24], magnetic tweezer[25], passive microrheology[26], and microdroplet-based sensors[27]. (iii) Elastography techniques, where the application of an external force is coupled with imaging techniques to measure displacement and back-calculate sample strain. These include optical stretching[28] and optical coherence elastography (OCE)[29,30]. Interestingly, many mechanical testing concepts have recently been combined with or adapted to microfluidics technology[31–34]. Each of these techniques has particular strengths and limitations, which have led to a specialization of their use for particular applications; for example, contact-based techniques are considered the gold standard when direct assessment of the Young's modulus of the cell and tissue samples is needed; bead-based techniques have been extensively used to extract the localized mechanical properties of the sample, mostly at the cellular and subcellular scales; elastography techniques are powerful to characterize and map the mechanical properties of biological tissue;

[1]Fischell Department of Bioengineering, University of Maryland, College Park, MD, USA. [2]These authors contributed equally: Jitao Zhang, Giuliano Scarcelli. ✉e-mail: jtzhang4@umd.edu; scarc@umd.edu

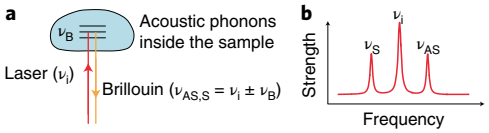

Fig. 1 | Principle of spontaneous Brillouin scattering. a, Brillouin scattering is caused by the interaction of the incident laser with acoustic phonons in the sample. **b**, A representative Brillouin spectrum. The subscripts 'S' and 'AS' indicate Stokes and Anti-Stokes components, respectively. 'V' represent the frequency.

and microfluidics-based techniques can assess the mechanical properties of cells in medium with high throughput.

In this context, an entirely different mode of probing material mechanical properties, via all-optical Brillouin light scattering, has been known and used for decades[35]. Since its invention, Brillouin spectroscopy has been a workhorse for noncontact material characterization. However, its application in the biological field has mostly remained limited to single-point measurements and ex vivo because of speed and sample damage limitations. Over the past ten years, due to the development of a faster spectroscopy strategy, confocal Brillouin microscopy has emerged as an imaging modality suitable for live biological samples[36], which allows noncontact, nonperturbative, label-free measurements[30,37,38]. Brillouin microscopy is an all-optical imaging modality in which a laser beam is used to probe the mechanical properties of the sample on the micron-level scale, and a 2D/3D mechanical image with diffraction-limited resolution can be acquired by scanning the sample in a confocal configuration[39]. We, along with colleagues from different laboratories around the world, have demonstrated non-perturbative characterization of numerous biological materials by Brillouin microscopy at both the cell and tissue level[39–51]. Although the technique is rapidly being recognized, a standardized approach for Brillouin microscopy has not been established, which is a significant obstacle to the widespread adoption of the technology. In this protocol, we aim to fill this gap and provide a robust approach for instrumentation, and data acquisition and analysis. By following this protocol, we expect that a reliable Brillouin microscope could be built by an engineer, postdoc, or graduate student with nonexpert optics knowledge and that high-quality data can be obtained by a nonspecialist user.

Development of the protocol

Brillouin microscopy is based on the physical process of spontaneous Brillouin scattering, where the interaction between the incident light and inherent acoustic waves inside a sample (generated by spontaneous thermal fluctuations) introduces a frequency shift (that is, Brillouin shift) to the out-going scattered light (Fig. 1a)[35]. A typical Brillouin spectrum features a central laser peak with a symmetrical Brillouin doublet (Stokes and anti-Stokes components) (Fig. 1b). Because the propagation of the acoustic wave is governed by the mechanical properties of the material, the Brillouin shift ν_B can probe the material's longitudinal modulus M' via the relationship

$$\nu_B = \frac{2n}{\lambda}\sqrt{\frac{M\prime}{\rho}}\sin\left(\frac{\theta}{2}\right), \quad (1)$$

where n and ρ are the refractive index and mass density of the material, λ is the light wavelength, and θ is the collection angle of the scattered light. Brillouin microscopy usually collects backward scattered light, thus $\theta = 180°$. The Brillouin shift of common materials is on the order of GHz, which corresponds to less than 0.01 nm in wavelength. To resolve such small frequency differences, common grating spectrometers used in fluorescence or Raman spectroscopy cannot be applied. Historically, Brillouin spectroscopy was enabled by the development of multipass scanning Fabry–Pérot (FP) etalon interferometry by Sandercock[52]. For decades, FP-based Brillouin spectroscopy has been used for material characterization[35] and remote sensing[53]. In biological fields, FP-based Brillouin spectroscopy measurements have been reported for collagen fibers[54–56], cornea and crystalline lens of the eye[57,58], biofilms[59], and bone[60]. However, these early demonstrations in the biological domain were single-point measurements and mostly ex vivo, because scanning FP spectrometers acquire the spectral components in a sequential manner and at low throughput, which typically results in long acquisition times (minutes) per Brillouin spectrum. Nonscanning FP spectrometers based on angular dispersion were subsequently demonstrated, which shortened the acquisition time[61] and enabled the first 2D Brillouin imaging of liquid-polymer samples[62]. However, angular-dispersive FP spectrometers remained fundamentally limited in terms of their throughput; thus, to increase the speed, they

sacrificed the ability to reject noise by limiting to single-pass operation. Thus, while Brillouin spectroscopy was widely utilized for noncontact material characterization, biological applications remained underexplored due to speed limitations and/or the high-power laser needed.

The instrument described in this protocol is the result of the past 15 years of optical development dedicated to address the speed and sample damage limitations for biological applications. The instrument is based on a different type of angular-dispersive etalon, viz. a virtually imaged phased array (VIPA), where the light is coupled into the etalon through a window and propagates forward after multiple reflections between the two surfaces of the etalon[63]. Since the entry surface of the VIPA has ~100% reflection while the output surface has partial reflection (>95%), all the light coupled into the etalon will be transmitted without forming a reflected interference pattern. In 2008, we demonstrated a Brillouin microscope using a VIPA-based Brillouin spectrometer, which allowed much higher throughput than the traditional FP etalon[36]. In subsequent years, a multistage VIPA-based Brillouin spectrometer was developed to improve the noise rejection ability at high throughput[64,65]. Meanwhile, other techniques such as destructive interference[66], absorptive gas chamber[67], spectral apodization[39], multistage FP filtering[68], and spectral coronagraphy[69] were developed to further reject non-Brillouin light components. In addition, the strength of the Brillouin signal has been improved by using an optimal excitation wavelength (660 nm) such that the acquisition time can be shortened without losing signal-to-noise ratio (SNR)[70]. Currently, the state-of-the-art Brillouin microscope described here has an acquisition time of 40 ms and can operate under shot-noise-limited condition with noise rejection of 75–80 dB, allowing it to measure nontransparent tissues[46,71,72] and monitor biological processes in situ[51].

Overview of the procedure

The procedure described in this protocol consists of six stages. First, we describe how to set up the microscope and add-on optics (Steps 1–10), where it is critical to install the setup in a standard laboratory room with minimal temperature fluctuations and choose the appropriate port of the microscope for beam coupling. Next, we describe how to build and optimize the Brillouin spectrometer (Steps 11–36), which are the most time-consuming stages of this protocol and require substantial attention. We then describe how to prepare samples for Brillouin measurements, taking NIH 3T3 cells as an example (Step 37). Next, we describe how to image the sample using the Brillouin microscope (Steps 38–44), in which periodical calibration is critical should the frequency drift of the laser be a concern. Lastly, we describe how to postprocess the data and present the results as 2D Brillouin images (Steps 45–48).

Applications of the method

Ocular biomechanics

The mechanics of the cornea is crucial for the variability in refractive processes and one of the main factors in eye diseases such as keratoconus[73]. Existing methods for quantifying corneal mechanics in vivo have low sensitivity and spatial resolution, and the results rely on multiple assumptions and modeling[74]. Brillouin microscopy provides a promising approach to address this clinical need, as it can provide a mechanical map of the cornea in vivo with high resolution and sensitivity[41,43,75,76]. Clinical data have shown that the Brillouin technique has potential for diagnosis and treatment monitoring of keratoconus patients[77]. In addition, Brillouin microscopy has demonstrated the feasibility of measuring the biomechanics of crystalline lens[40,78,79] and retina[80].

Developmental biomechanics

The morphological evolution during embryo development involves cell alignment and folding as well as tissue reshaping and patterning, accompanied by dramatic mechanical changes of embryonic tissue[4,81]. As a noncontact technique, Brillouin microscopy has shown enough sensitivity and spatial resolution to quantify the tissue mechanics of both mouse and zebrafish embryos[72,82]. Specifically, this technique has demonstrated possible applications in biologically relevant processes, such as neural tube closure[51], development and injury of spinal cord[45], and epithelial cell differentiation across the corneal surface[48].

Cellular biomechanics

Mechanical cues from the microenvironment, together with gene expression and signaling pathways, regulate cell functions and activities through the mechanism of mechanotransduction[83,84].

In response, cells alter their mechanical properties, suggesting that mechanical signatures are promising indicators of cell behaviors. In 2015, we reported 3D mechanical mapping of live cells and revealed the mechanical changes due to cytoskeletal modulation and cell volume regulation using Brillouin microscopy[39]. Brillouin microscopy was then applied to quantify the subcellular mechanical properties of both live animal and plant cells[44,47,85–87]. Brillouin microscopy is also suitable to assess the mechanical properties of the nucleus, which is embedded in the surrounding cytoplasm and not directly accessible to traditional methods[88]. Using the Brillouin technique, we revealed that the nuclear mechanics is regulated by both the cytoskeletal network and internal nanostructures[51], which can help understand how the intracellular mechanisms alter the nuclear mechanics and thereby affect cell behaviors in physiological and pathological conditions.

Cancer metastasis and 3D tumorigenesis

Substantial evidence has shown that cancer cells have altered mechanical properties compared with healthy cells[33,89]. Specifically, metastatic cancer cells are usually softer (more deformable) than noncancer ones[90–94]. In this context, we revealed that nuclear mechanics is a crucial regulator when tumor cells migrate through a confined region, which represents a key step in the metastatic cascade[95]. In addition, Brillouin microscopy has been validated for monitoring the biomechanics of 3D nodules and tumoral tissues[49,50], paving the way for the study of tumor progression and drug therapy using 3D in vitro models.

Biomaterial characterization

The noncontact and noninvasive features of the technique may open up new possibilities for material characterization that are challenging with conventional methods; For example, the Brillouin spectroscopy technique allowed the first ever quantification of the entire stiffness tensors of spider silk, whose diameter is small, and the linear elastic properties could be altered upon mechanical deformation[96]. In addition, the Brillouin technique has been used to characterize the mechanical properties of other biomaterials, such as collagen[97], fibrous proteins of the extracellular matrix[98], protein crystals[99], and hydrogels[100–102].

Medical applications

In addition, it has been suggested that Brillouin microscopy could be a useful tool for a variety of medical applications, such as Barrett's esophagus[98], atherosclerosis[103], bacterial meningitis[104], Alzheimer's disease[105,106], obesity[107], amyotrophic lateral sclerosis[47], melanoma[108], and dental diagnostics and restoration[109].

Comparison with other methods

FP etalon-based Brillouin spectroscopy

The VIPA-based Brillouin microscopy described in this protocol is based on the same physical process of spontaneous Brillouin scattering as FP etalon-based spectroscopy. The main difference between the two instruments lies in the spectral dispersion element. Although both the FP and VIPA use a parallel etalon to disperse light, the FP etalon has intrinsically lower throughput because it forms an interference pattern in both transmission and reflection. For practical applications, the reflected pattern represents a significant loss of signal which increases as the finesse (and thus spectral resolution) of the spectrometer increases. Of note, clever attempts to remediate this issue by recirculating the reflected light have been demonstrated recently[110]. The VIPA etalon overcomes this throughput issue by including a particular surface coating: the entry surface of the VIPA has ~100% reflection, other than a small antireflection (AR) window for coupling the input beam, while the output surface has partial reflection (>95%). As a result, all the light coupled into the etalon will be transmitted without forming a reflected interference pattern, resulting in an increase in the throughput on the order of the interferometer finesse. In addition, the nonscanning configuration allows the VIPA to acquire the entire spectrum in one shot, while an FP etalon must acquire each spectral component in sequence by physically scanning the cavity of the etalon. Considering these factors, a typical VIPA-based spectrometer is much faster than a FP etalon-based spectrometer. On the other hand, FP-based spectrometers can be tuned to allow finer spectral analysis with better linewidth. In addition, the multipass multistage FP-etalon spectrometer can provide higher spectral extinction (>150 dB) than the highest demonstrated with VIPAs (85 dB)[64,68,111]. This extra extinction is valuable for the characterization of highly reflective materials such as metals; however, for biological applications,

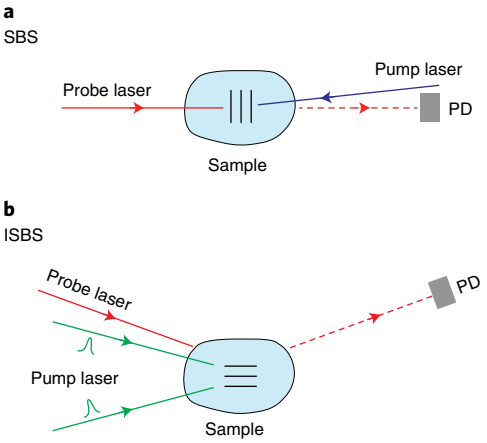

Fig. 2 | Schematics of SBS and ISBS. The dashed line represents the output laser beam containing the Brillouin signal of the material. The line set inside the sample indicates the excited acoustic phonons. PD, photodetector.

current VIPA-based spectrometers have sufficient extinction to operate in the shot-noise-limited regime, even in opaque tissues or very close to the reflective interfaces. In short, as a pioneering Brillouin technology, FP-etalon-based Brillouin spectroscopy is still actively used in biological applications today[96,98,112,113]. However, because the spectral acquisition of the scanning FP etalon is slow, this technique is mostly limited to single- or few-point analysis.

Stimulated Brillouin scattering (SBS) microscopy

This technique is based on stimulated Brillouin scattering, in which acoustic phonons are excited by two counterpropagating continuous-wave (CW) lasers[114] (Fig. 2a). Since the stimulated process has higher scattering efficiency, the generated Brillouin signal can be much stronger than in the case of spontaneous Brillouin scattering[115–117]. As such, the acquisition time of SBS microscopy can potentially be shortened in comparison with spontaneous confocal Brillouin microscopy. Its additional advantages include higher spectral resolution and less background elastic scattering noise, which enables measurements of linewidth and Brillouin strength, which in turn can provide viscosity and density information. Very recently, the first biological application of SBS microscopy was demonstrated by mapping live *Caenorhabditis elegans* samples[118]. However, current SBS microscopy demonstrations use CW lasers and thus do not fully exploit the advantage of the nonlinear effect and need high laser powers to reach the threshold of the stimulated process. Consequently, potential phototoxicity is a concern for biological samples exposed to such high laser powers. While *C. elegans* has been shown to be little affected by SBS mapping, the photodamage to other biological samples should be carefully evaluated before implementing this technique, as the phototoxic effect strongly depends on the sample used. In addition, such measurements must be implemented in a transmission geometry, thus requiring access to the sample from both sides.

Impulsive stimulated Brillouin scattering (ISBS) microscopy

This technique is also based on the stimulated scattering process, but an ultrashort pulse laser is used to excite acoustic phonons[119] (Fig. 2b). In the implementation of ISBS microscopy, acoustic phonons are generated within the interference pattern of a pulsed pump laser and detected by a probe laser under the Bragg diffraction condition[120,121]. Currently, the spatial resolution of ISBS microscopy does not reach single-cell level (lateral 10 μm, axial 230 μm) due to the optical configuration, and the setup must be implemented in a transmission geometry. The technique has been validated by measuring liquid samples and hydrogels, but biological applications have not been reported so far.

Limitations

The mechanical property probed by the Brillouin technique via the Brillouin shift is the microscopic high-frequency longitudinal modulus within the sample. This quantity is not the same as the quasistatic elastic modulus (for example, the Young's modulus or shear modulus) measured by conventional stress–strain methods on macroscopic samples. Currently, there is no theoretically

established relationship between the two moduli. However, strong correlations have been observed in many physiological and pathological processes[39,40,50,51,75,122], which are expected because most material changes alter both moduli in the same direction. For highly hydrated gels (~95% water content) and large hydration variations, the Brillouin shift is dominated by the change of the water content and is thus no longer a reliable estimator of the conventional elastic modulus[123,124]; instead, in the regime of cells and tissues (~70% water content), Brillouin technology can be used to estimate traditional mechanical properties after building a correlation working curve between the two moduli[39].

Currently, the pixel dwell time of the Brillouin microscope is 40–100 ms, which is slow in comparison with other imaging modalities such as confocal fluorescence microscopy. This is because the Brillouin signal generated by the spontaneous scattering process is intrinsically weak. Increasing the input laser power could reduce the dwell time and thus improve the speed. However, high laser powers may introduce photodamage via absorption of the incident light by the sample, thus the ultimate improvement in this respect is limited[70]. As a result, for large samples, the acquisition time could become a crucial limiting factor and should be considered carefully.

The sensitivity of the instrument is limited by the spectral precision of the spectrometer. As demonstrated in the procedures, the spectral precision of the described instrument is ~8 MHz for the measurement settings analyzed here (Fig. 8). Considering that biological samples typically have a Brillouin shift of ~6 GHz, the relative precision of the Brillouin frequency is ~0.13%. According to the relationship between the longitudinal modulus and Brillouin shift (Eq. 1), the relative precision of the longitudinal modulus is thus 0.26%. This translates into a precision for the estimation of the Young's modulus on the order of a few percent according to the quantified correlation of the two moduli in cells and tissues[39,40,51].

The calibration method used in this protocol assumes that the spectral dispersion is constant across the spectral pattern, which, however, is not exactly true in practical scenarios. As the dispersion is related to the angle of the light within the VIPA cavity, higher-order dispersion will have less displacement on the electron-multiplying charge-coupled device (EMCCD) camera[125]. Consequently, Brillouin components from adjacent dispersion orders have slightly different spectral dispersion, which results in a nonlinearity of the VIPA pattern and may introduce artifacts into the calibration results. If the Brillouin shift of a sample is far from those of the calibration materials, an inaccuracy in the derived Brillouin shift may be observable. In this case, more standard materials whose known Brillouin shifts cover a broader region of the spectral pattern can be used for calibration[126], and the calibration parameters can be obtained by fitting multiple Brillouin peaks using a polynomial function.

The spatial resolution primarily depends on the voxel size of the focused laser beam, which is determined by the diffraction limit of the optical system, and thus by the numerical aperture (NA) of the objective lens (objective 1) chosen in the experiment. For objective lenses with high numerical aperture, the spatial resolution will also be affected by the mean free path of the acoustic phonons[127]. Therefore, the mechanical properties of samples smaller than the spatial resolution will not be resolved by the Brillouin microscope. Instead, the output result will be the averaged Brillouin shift of all the material within that voxel. In practice, this limits the ultimate mechanical resolution of Brillouin microscopy to the order of 1 micron.

The penetration depth of the Brillouin microscope depends on the transparency of the sample; at the demonstrated spectral extinction, the Brillouin confocal microscope has similar penetration depth to reflectance confocal microscopy. In practice, this corresponds to ~200 μm of mouse embryo at 532 nm (ref. [46]), >500 μm of zebrafish embryo at 780 nm (ref. [45]), 360 μm of retina at 532 nm (ref. [80]), ~90 μm of tumor nodules at both 532 nm and 660 nm (ref. [50]), and 100 μm of chicken muscle tissue at 532 nm (ref. [68]).

To avoid any crosstalk, the optical path for the Brillouin channel and the fluorescence channel are physically separated. As such, Brillouin and fluorescent images are acquired in sequence rather than simultaneously. Although this will slightly increase the overall acquisition time, the accuracy of the image coregistration in the data postprocessing is not affected.

The add-on optics in this protocol are designed for a specific commercial microscope (IX81, Olympus); depending on the configuration of different microscopes, adjustments to the optical setup may be required to ensure that the protocol works as expected.

Expertise needed to implement the protocol

A skilled engineer or applied physicist, graduate student, or postdoc with an optics background and experience of optical alignment should be able to build the instrument within 5–9 days by carefully

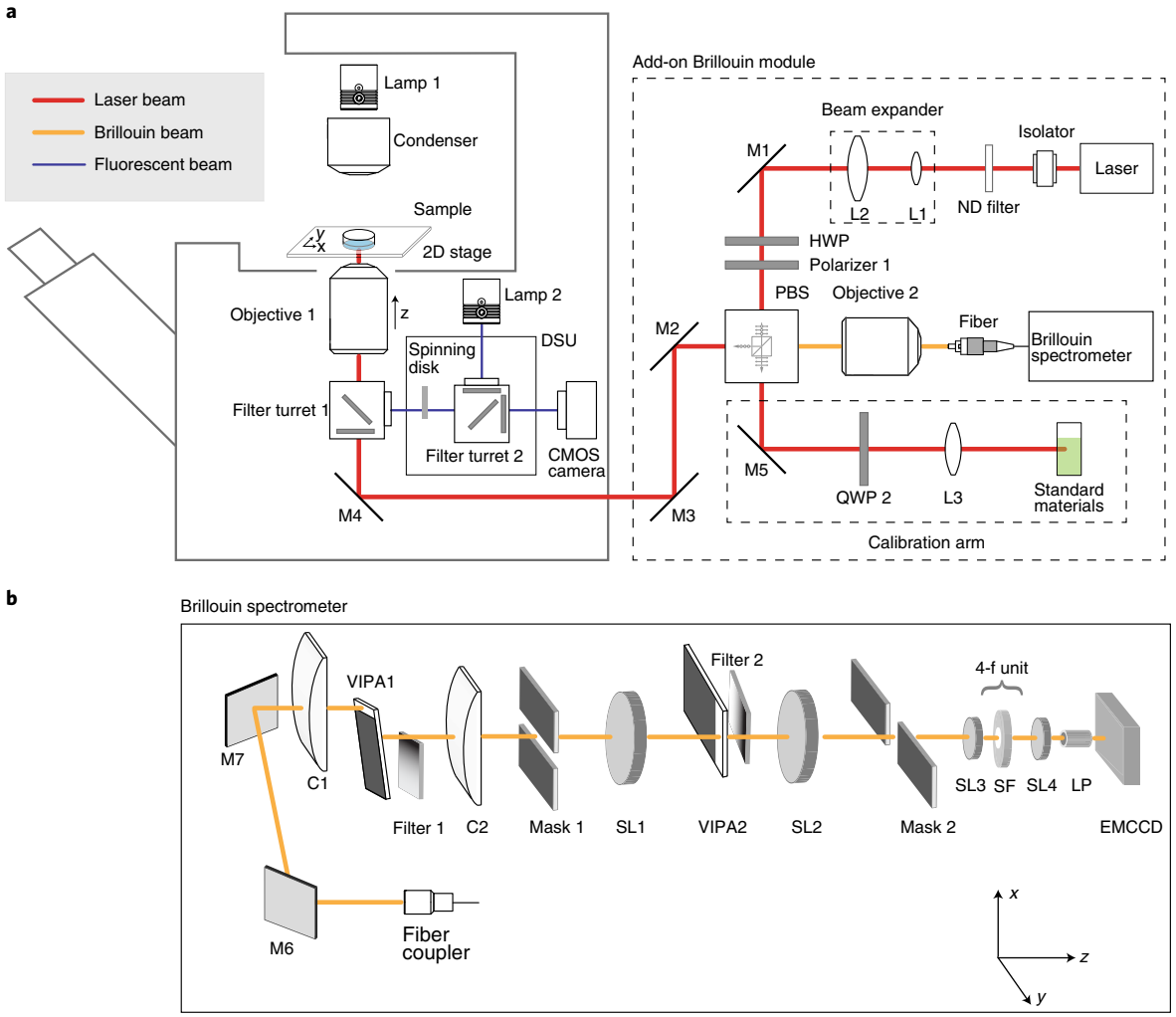

Fig. 3 | Schematic of the confocal Brillouin microscope. a, Integration of a confocal microscope and the add-on Brillouin module. Filter turret 1/2, commercial microscope turret for housing the fluorescence filter cubes; DSU, disk spinning unit; ND filter, neutral density filter; M1, M2, M3, M5, reflection mirrors; M4, dichroic mirror. HWP, half-wave plate; PBS, polarized beam splitter; QWP, quarter-wave plate. **b**, Optical design of the Brillouin spectrometer. M6, M7, reflection mirrors; C1, C2, cylindrical lenses; SL1–SL4, spherical lenses; SF, spatial filter; LP, lens pair; EMCCD, electron-multiplying charge-coupled device; filter 1/2, linear variable ND filters.

following this protocol. An undergraduate student with computer engineering background and experience of LabVIEW-based programming should be able to develop the software interface within a month. It is expected that a nonspecialist user will be able to optimize and run the instrument to obtain high-quality data after necessary training (2–4 weeks). All these estimates are based on our experience training instrument builders and users.

Experimental design

Instrumentation

The instrument includes a commercial inverted confocal microscope (e.g., IX81 + disk spinning unit (DSU), Olympus) and a homemade add-on Brillouin module (Fig. 3). To briefly describe the operation of the commercial microscope, lamps 1 and 2 are light sources for bright-field and fluorescent imaging, respectively. For both bright-field and fluorescent/confocal imaging, filter turret 1 is set to a 45° mirror to direct light to/from the DSU, which consists of filter turret 2 and the spinning disk. A complementary metal–oxide–semiconductor (CMOS) camera (Neo, Andor) is installed on the DSU to acquire both bright-field and fluorescent/confocal images. For sample translation, the microscope is equipped with a 2D translational stage (Prior Scientific) for holding and scanning the sample in the *x*–*y* plane. Scanning along the *z*-axis is achieved by moving the objectives (objective 1) with the microscope's own stage.

The add-on Brillouin module includes a CW laser source, an optical setup outside the microscope body, a Brillouin excitation/emission "filter cube" to guide light into and out of the microscope body, and a Brillouin spectrometer. The Brillouin filter cube is a home-made customized mount to fit a slot on the commercial microscope's turret which usually houses the fluorescence filter cubes. To enable the Brillouin measurement 'channel,' the Brillouin filter cube is easily placed into the beam path by rotating filter turret 1.

The laser source should have a single-frequency output with a narrow bandwidth (<1 MHz), excellent spectral purity (>60 dB), and good frequency stability (<0.2 GHz in 0.5 h). In this protocol, a 660-nm laser (Torus, Laser Quantum) was used as the light source. After passing through an optical isolator, neutral-density (ND) filter, beam expander (designed such that the output beam can overfill the back focal aperture (BFA) of objective 1), and a half-wave plate, the laser beam goes through a polarized beam splitter (PBS). Depending on the polarization of the incoming light, controlled by polarizer 1, the PBS guides the beam to either mirror M2, for Brillouin measurements of samples, or M5, for Brillouin measurements of calibration materials. For Brillouin measurements of samples, the laser beam is coupled into the microscope body through its right-side port via mirrors M2 and M3. Then the beam is focused into the sample after passing through mirror M4, the Brillouin filter cube (installed on a free slot of filter turret 1), and the objective lens (objective 1). The backward-scattered Brillouin light is collected by the same objective. Since the input laser and Brillouin signal have nearly identical wavelengths, no traditional filter or dichromatic mirror can be used to separate the two. For this reason, the Brillouin filter cube contains a quarter-wave plate (QWP), which allows orthogonal linear polarizations to be conferred on the input laser and backward-scattered Brillouin signal for their separation at the PBS. The Brillouin-scattered light is transmitted through the PBS to a second objective lens (objective 2), which couples light to the Brillouin spectrometer through a single-mode fiber. For calibration purposes, the initial polarization of the laser beam can be rotated by 90° so that it is transmitted through the PBS to the calibration arm instead of the microscope body. In the calibration arm, the beam first passes through a QWP2 and is focused into the reference material under examination by the positive lens L3. The scattered Brillouin light traces its path back, is reflected at the PBS, and is coupled into the fiber by objective 2 to be analyzed by the Brillouin spectrometer.

The choice of objective 1 depends on the smallest length scale that one wants to observe, and its NA primarily determines the spatial resolution of the Brillouin microscope. Since the Brillouin scattering is a result of the interaction between light and acoustic phonons, the actual resolution of Brillouin imaging will also be affected by the propagation of the acoustic wave, which can be quantified by the wavelength and the mean free path of phonons within the sample[127]. Therefore, the length scales of both the optical beam and the acoustic wave should be taken into consideration when estimating the mechanical resolution. To ensure confocality and maximize the collection of the Brillouin signal at the fiber port, objective 2 is chosen such that the output beam matches the NA of the single-mode fiber. Since the diameter of the collected Brillouin beam is determined by the BFA of objective 1, which is usually smaller than the BFA of objective 2, the effective NA of objective 2 is scaled by BFA_2/BFA_1. Taking the choices of this protocol as an example, as objective 1 (40×, 0.6 NA) has $BFA_1 = 5.4$ mm and objective 2 (10×, 0.25 NA) has $BFA_2 = 9$ mm, the effective NA of objective 2 becomes 0.15, which is close to the NA (0.1–0.14) of the fiber. Alternatively, the beam expander consisting of L1 and L2 can be designed such that the size of the outcoming laser beam matches the BFA of objective 2 to optimize the fiber coupling, and an additional beam expander can be placed between the PBS and the microscope body to match the BFA of objective 1. In case the microscope port with a tube lens is used for the coupling of the add-on Brillouin module, the tube lens itself can be part of the additional beam expander, then only one more lens is needed to adjust the beam size at the BFA of objective 1.

The Brillouin spectrometer (Fig. 3b) features two stages with orthogonally oriented VIPAs (free spectral range (FSR) 15 GHz, LightMachinery). The outcoming light from the fiber is coupled into VIPA 1 by cylindrical lens C1 in the vertical direction, and the spectral pattern at the output of VIPA 1 is projected onto mask 1 by cylindrical lens C2. The spherical lens SL1 then couples the pattern on mask 1 into VIPA 2 in the horizontal direction, and spherical lens SL2 projects the spectral pattern at the output of VIPA 2 onto mask 2. After being relayed by a 4f system consisting of spherical lenses SL3 and SL4 and spatial filter SF[69], the spectral pattern is imaged onto the EMCCD camera (iXon, Andor) by lens pair LP. To improve the extinction of the spectrometer, linear variable ND filters (filters 1 and 2) are placed immediately after the VIPAs as apodization filters to convert the intensity profile of the VIPA pattern from an exponential to Gaussian shape[39].

Alternatives for key equipment

1 Microscope body. This protocol can be adapted to other inverted microscopes from different manufacturers. For a microscope body with an infinity port (e.g., Leica DMi8), which can guide the laser beam to objective 1 without a tube lens, the add-on Brillouin module can be coupled into the microscope through the infinity port without any change. For other microscopes (e.g., Zeiss Axiovert or Nikon Eclipse Ts2R), the imaging port (side port) instead can be used for coupling. In this case, since the laser beam has to pass through a tube lens before reaching objective 1, an additional lens can be inserted between M3 and M4 for relaying purposes. This lens has the same focal length as the tube lens and is placed at twice the focal length of the tube lens, so that it and the tube lens together form a 1:1 imaging system to ensure that the laser beam after the tube lens is collimated and has the same diameter as before M3.

2 Laser source. As mentioned above, to obtain high-quality Brillouin data, the spectral linewidth, purity, and frequency stability are crucial parameters for choosing a laser source. Beyond that, the trade-off between the scattering efficiency and possible phototoxicity should be considered when choosing the wavelength[70]. Shorter wavelengths (e.g., 532 and 561 nm) will provide a higher Brillouin signal than longer wavelengths (e.g., 660, 671, and 780 nm) because the scattering efficiency is proportional to λ^{-4}, but the light absorption by melanin, hemoglobin, and lipid in cell and tissue at short wavelengths may introduce significant photodamage when the laser power is high[128]. On the other hand, absorption by water will be dominant in the infrared region. Another advantage of using a short wavelength is to achieve better spatial resolution. The wavelength used in this protocol is not the only choice but rather a compromise considering the signal strength and the photodamage. In fact, the feasibility of other wavelengths has also been demonstrated for different applications[40,47,48,86,96,129,130].

3 Brillouin spectrum camera. When choosing a camera, several parameters should be considered, including the dark current, read noise, quantum efficiency, and pixel readout rate. As the signal from spontaneous Brillouin scattering is relatively weak, a camera with a low noise level and high quantum efficiency is preferred. In this protocol, an EMCCD camera is recommended for the best performance. We notice that a scientific CMOS (sCMOS) camera has also been used in Brillouin spectrometers[86,111]. In comparison with the EMCCD (e.g., iXon Ultra 897, Andor), the sCMOS camera (e.g., Neo 5.5, Andor) has only 60% quantum efficiency but >20 times the dark current. On the other hand, the sCMOS device has much a higher pixel readout rate than the EMCCD. Taken together, a sCMOS camera can be considered when the Brillouin signal is fairly strong and fast acquisition is desired.

4 The FSR of the VIPA. The range of Brillouin shift that can be measured unambiguously by the spectrometer is about half of the FSR of the VIPA. The choice of the FSR in this protocol is based on the fact that most cells and some tissue samples (such as cornea and early-stage embryoes) have a Brillouin shift in the range of 6–7 GHz at 660 nm. For very stiff biological samples, such as crystalline lens[40], fibers[96], cartilage[98], and bone[131,132], a VIPA with a larger FSR is needed.

Brillouin spectrum and calibration

After dispersion by a VIPA etalon, the input light is separated in space on the basis of its frequency (Fig. 4a). The spectral pattern imaged onto the EMCCD camera could include multiple dispersion orders. Each order features a triplet (laser peak, Stokes, and anti-Stokes Brillouin peaks), where the successive orders are spaced by a frequency spectral range (FSR) (Fig. 4b). In most cases of experiments, the intensity of the laser peak will be much higher than the Brillouin signal because of the light reflection at the interface as well as the strong scattering in nontransparent samples. As such, the camera can easily be saturated by the overwhelming laser peaks, thus distorting or even burying the weak Brillouin signal. To avoid this, instead of using a single triplet to determine the Brillouin shift ν_B, we use the anti-Stokes Brillouin peak from one dispersion order and the Stokes Brillouin peak from the successive order, as shown in the highlighted region of Fig. 4b, while all the remaining peaks are blocked by masks 1 and 2 within the spectrometer. With the measured peak separation ΔD and the calibrated FSR, the Brillouin shift ν_B can readily be determined as

$$\nu_{\mathrm{B}} = \frac{\mathrm{FSR} - \Delta D}{2}. \tag{2}$$

Since the peak separation recorded on the camera is counted in pixels, the pixel-to-frequency conversion ratio (PR) must be calibrated to calculate ΔD.

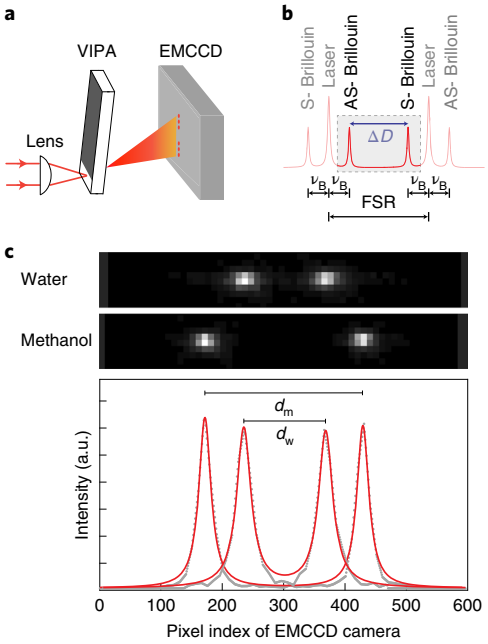

Fig. 4 | Brillouin spectrum acquisition and calibration. a, Principle of VIPA-based spectrometer. **b**, Brillouin spectrum acquired by a double-stage VIPA spectrometer. FSR, free spectral range. The dashed square indicates the region acquired by the camera. **c**, Acquired Brillouin spectra of standard materials and the intensity profiles after curve fitting. d_m and d_w are the peak separation of the Brillouin spectrum for methanol and water, respectively. Dots are raw data; red lines are fit curves.

In the calibration process, the Brillouin spectra of two standard materials with known Brillouin shift (e.g., water and methanol) are acquired through the calibration arm, and the results are then used to determine the two unknown parameters (FSR and PR) through the relationship

$$\mathrm{FSR} - \mathrm{PR} \cdot d_w = 2\nu_w \tag{3a}$$

$$\mathrm{FSR} - \mathrm{PR} \cdot d_m = 2\nu_m \tag{3b}$$

where d_w and d_m are the peak separations of the Brillouin signals from the water and methanol samples, respectively, which are determined from the acquired spectra (Fig. 4c). The above process assumes that the laser frequency is constant. In practice, the distinct drift of the laser frequency could introduce artifacts when applying a single calibration result to experimental data collected over a long time. In this case, more frequent calibrations during the experiment are needed to obtain reliable data. To achieve this, polarizer 1 is installed on a motorized rotation mount, and a motorized flip mirror is placed after L3 and set at 45° to the optical path for switching between standard materials. Periodical calibration (e.g., every 0.5 h) can be implemented by automatically controlling the motorized mounts using a computer program.

A high-NA objective lens will introduce a small shift of the Brillouin peak (e.g., 2% at NA 0.8) and a distinct broadening of the spectral full-width at half-maximum (FWHM)[133]. In this protocol, the collection NA of the reference arm (NA 0.14) is smaller than that of the measurement arm (NA 0.6), but the calibration error caused by the peak shift (<1%) can be neglected. However, if a higher-NA objective lens is used in the measurement, the potential artifact might need to be considered and direct comparison of Brillouin data collected from low and high NA based on the same calibration arm should be careful. In case this is a concern, we recommend matching the NA of both arms to remove this artifact.

Sample preparation

The sample is usually placed on a glass-bottomed Petri dish with small amount of culture medium. For easier measurements, it is suggested, if possible, to coat the bottom of the dish with a thin hydrogel layer before seeding the sample to avoid strong reflection at the interface between the glass and medium. The thickness of the layer can be adjusted on the basis of the working distance of the objectives (objective 1) and the thickness of the sample. For long-term live imaging, the dish can be

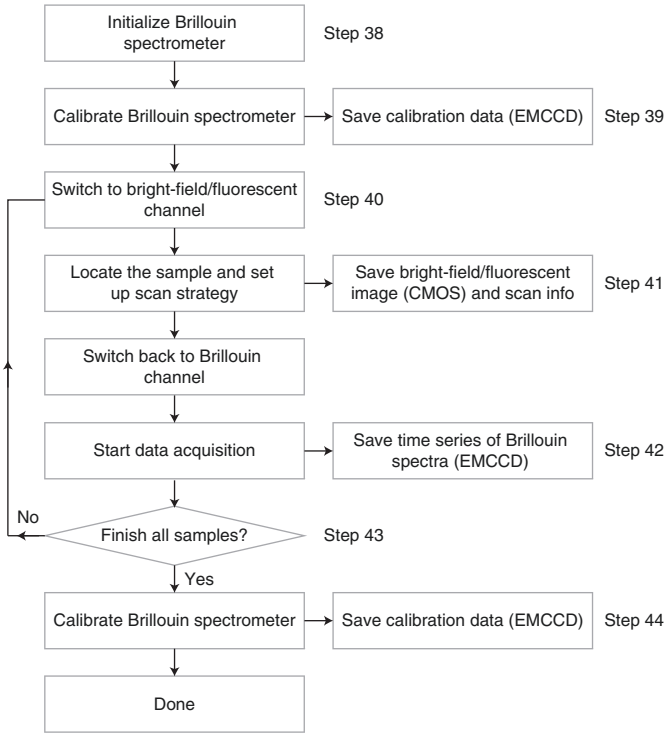

Fig. 5 | Flowchart of the data acquisition process for Brillouin imaging.

housed in a mini-incubator designed for use with a microscope to control the temperature, humidity, and CO_2 level.

Data acquisition

The data acquisition is implemented by a homemade LabVIEW script (Supplementary Fig. 1), and the procedure is shown in a flowchart in Fig. 5. In the initialization of the spectrometer, the tilt angle of the VIPAs must be carefully adjusted to both maximize the signal and balance the intensity of the two peaks. In spectrometer calibration, multiple samplings (e.g., $n = 300$) are taken for each standard material. Next, the optical path is switched to the bright-field or fluorescent channel by rotating filter turret 1 (Fig. 3a). Next, when the sample of interest is located in the field of view, the scanning strategy is chosen in terms of the scanning plane (e.g., *x*–*y*, *x*–*z*, or *y*–*z*), range, step size, and the exposure time of the EMCCD camera. After the optical path is switched back to the Brillouin channel, the data acquisition is launched. During this step, the Brillouin spectrum at each position of the sample is captured and saved as a figure file for data postprocessing. To monitor the status of the measurement in real time, the corresponding Brillouin shift is obtained by fitting the spectrum using a Lorentzian function, and the value is displayed as a pixel of a color image in the LabVIEW program. When a measurement session is completed, it is advisable to calibrate the spectrometer again, because the fluctuation of the laser frequency as well as the mechanical drift of the VIPAs may introduce artifacts into the results. Depending on the frequency stability of the laser and the measurement time for each sample, spectrometer calibration should be implemented whenever such drift is suspected.

Data postprocessing

We use MATLAB to process the raw data (example codes as well as representative raw data are provided in Supplementary Data 1). The key procedures are summarized in Fig. 6. First, the FSR and PR are calculated using equation (3) for each sampling point of the calibration data, and the average is used as the final value of the parameters for retrieving the Brillouin shift of the sample. For same-day experiments, it is important to check the values of FSR and PR from all the calibration datasets. In case any drift is observed, the values obtained from the nearest calibration dataset should be used for retrieving the Brillouin shift of the related measurements. From the 1D vector of retrieved Brillouin shifts, a 2D Brillouin image can be reconstructed using the scanning range and step size. Further analysis can be performed by coregistering the Brillouin image with a corresponding

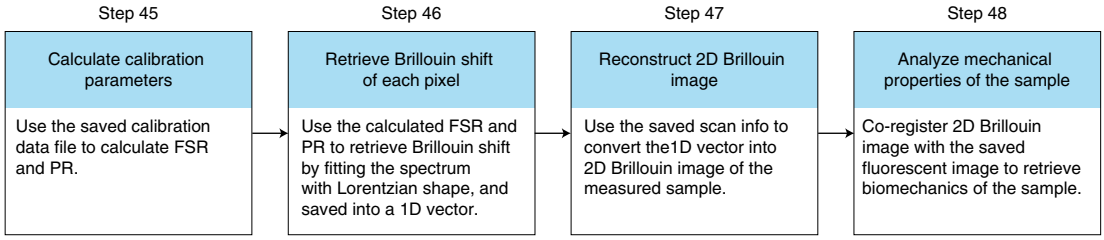

Fig. 6 | Flowchart of the data postprocessing.

fluorescence image, enabling the extraction of the Brillouin shift of either the whole sample or any subregion of interest. Furthermore, using the known refractive index and mass density of the sample, the longitudinal modulus derived by the Brillouin shift can be obtained via equation (1).

Materials

Biological materials

- Cells of interest—any adherent cells should work with the method described in the protocol, such as NIH 3T3 fibroblast cells (ATCC, cat. no. CRL-6442, RRID: CVCL_0594) **! CAUTION** The cell lines used for your research should be regularly checked to ensure that they are authentic, not cross-contaminated, and not infected with mycoplasma.

Reagents

- Methanol (Thermo Fisher Scientific, cat. no. A453-500) **! CAUTION** Methanol is highly flammable and toxic. When handling methanol, avoid direct exposure by wearing gloves and cover the lid of the container properly.
- Deionized water (Thermo Fisher Scientific, cat. no. LC267402)
- Cell culture media. For NIH 3T3 cells, we use DMEM (Thermo Fisher Scientific, cat. no. 11995065) with 10% (vol/vol) fetal bovine serum (Thermo Fisher Scientific, cat. no. 30-2020) and 1% (vol/vol) penicillin–streptomycin (Thermo Fisher Scientific, cat. no. 15070-063)
- (Optional) Hydrogel, for example, polyacrylamide (MilliporeSigma, cat. no. GF61308536-1EA)
- (Optional) Fluorescent dyes, for example: Hoechst 33342 (Thermo Fisher Scientific, cat. no. 62249)

Equipment

- Optical table (e.g., 4 × 6 ft, Newport, cat. no. INT4-46-8-A)
- Microscope body (Olympus, IX81+DSU)
- Motorized 2D stage for optical microscope (Prior Scientific, cat. no. H117E2)
- Objective lens (objective 1: Olympus, cat. no. LUCPLFLN40X; objective 2: Thorlabs, cat. no. RMS10X)
- EMCCD camera (Andor, iXon 897)
- CMOS camera (Andor, Neo 5.5 sCMOS)
- VIPA (FSR 15 GHz, LightMachinery, cat. no. OP-6721-6743-3)
- Holder for VIPAs (Thorlabs, cat. no. KM100C, x2)
- Mount adapter for EMCCD camera and lens pair (Thorlabs, cat. no. SM1A39)
- Laser source (Laser Quantum, torus 660)
- Isolator (Thorlabs, cat. no. IO-5-670-HP)
- ND filter (Thorlabs, cat. no. NDC-25C-4)
- Beam expander (f_1 = 16 mm, Thorlabs, cat. no. AC080-016-B-ML; f_2 = 100 mm, Thorlabs, cat. no. AC254-100-B-ML)
- Mirrors (M4: Chroma, cat. no. T660dcrb; all the rest: Thorlabs, cat. no. BB1-E02-10)
- Polarizer (Newport, cat. no. 10LP-VIS-B)
- Half-wave plate (Thorlabs, cat. no. WPH10M-670)
- Quarter-wave plate (Thorlabs, cat. no. WPQ10M-670, x2)
- Polarized beam splitter (Thorlabs, cat. no. CCM1-PBS252)
- Single-mode fiber (Thorlabs, cat. no. P1-460Y-FC-2)
- 3D translational stage (Thorlabs, cat. no. MBT616D)
- Lens for calibration arm (f_1 = 45 mm, Thorlabs, cat no. AC254-045-B-ML)
- Optical components for Brillouin spectrometer (all from Thorlabs. Fiber coupler, f = 11 mm, cat. no. PAF2P-11B; cylindrical lens (×2), f = 200 mm, cat. no. LJ1653L1-B; spherical lens (×2), f = 200 mm,

cat. no. AC508-200-B; spherical lens (×2), f = 40 mm, cat. no. AC254-040-B-ML; lens pair, MAP103030-B; variable ND filter (×2), cat. no. NDC-25C-4)
- Slits for masks (Thorlabs, cat. no. VA100)
- Iris and 2D translation mount for spatial filter (Thorlabs, cat. no. SM1D12, cat. no. CXY1)
- 1D translational stages (Newport, cat. no. 423, ×9)
- Vertical stages (Edmund Optics, cat. no. #66-499, ×3)
- Components for building the optical enclosure (all from Thorlabs: rails, cat. no. XE25L09, XE25L12; black hardboard, cat. no. TB4; blackout fabric, cat. no. BK5; black masking tape, cat. no. T137-2.0)
- Cuvette for holding standard liquid materials (Thorlabs, CV10Q3500F)
- Petri dish (35 mm, glass bottom, Thermo Fisher Scientific, cat. no. NC9732969)
- MATLAB software (version R2020a, MathWorks, https://www.mathworks.com)
- MATLAB example codes (Supplementary Data 1)
- LabVIEW software (version 2016, National Instruments, https://www.ni.com/en-us/shop/labview.html)

Alignment tools
- Power meter (Thorlabs, cat. no. PM130D)
- Shearing interferometer (Thorlabs, cat. no. SI050, SI100P)
- Home-built alignment assembly (Step 6), including irises (Thorlabs, cat. no. SM1D12C, ×2), cage plates (Thorlabs, cat. no. CP33, ×3), cage assembly rods (Thorlabs, cat. no. ER18, ×4), and threading adapters (Thorlabs, cat. no. SM1A4, SM1T2)

Customized components
- Mount for Brillouin filter cube (Supplementary Data 2)
- Mounting base for laser head, including three stacked plates (Supplementary Data 3)
- Mounting stand for EMCCD camera, including base component, front component, circle component, and spacers for height adjustment (Supplementary Data 4)

Procedure

Setting up the microscope and add-on optics ● Timing 2–4 d

1 Install and fix the microscope body on the optical table, placing it ~3 ft from the right short end and 2 inches from the bottom long side, and facing to the top long side of the table (Supplementary Fig. 2).

▲ **CRITICAL STEP** Since the frequency stability of the laser and mechanical mounts inside the spectrometer are sensitive to the environmental temperature, the setup should be installed in a standard laboratory room with minimal temperature fluctuation. Thermally stabilized mounts can be used when temperature fluctuation is a concern.

2 Place the laser head near the right short end of the table and install it on the customized aluminum base. The height of the base is determined such that the laser beam ultimately has the same height as the center of the right-side port of the microscope. Alternatively, a periscope optical arrangement would be needed to facilitate coupling the laser beam into the microscope body. Adjust the orientation of the laser head such that the output laser beam roughly aligns with the table holes. Install the isolator in front of the laser head. Install a variable ND filter after the isolator and adjust the laser power to the minimum visibility for alignment.

3 Install the beam expander, including lens L1 (f_1 = 16 mm) and L2 (f_2 = 100 mm), immediately after the ND filter. Place L2 on a 1D translational stage. Finely adjust its position to make the output beam collimated, which can be checked by using a standard shear plate interferometer (Thorlabs). The magnification of the beam expander (f_2/f_1) is chosen by considering both the size of the laser beam and the BFA of objective 1. Here, the size of the laser beam is ~1.8 mm, and it becomes 11.25 mm after expansion so that the beam can overfill the BFA of several common objectives. In case a different laser source and/or objective 1 are used, the combination of L1 and L2 must be adjusted accordingly.

4 Install mirror M1 ~450 mm away from the laser. Set the mirror at ~45° versus the incoming laser beam so that the reflected beam aligns with the table holes. Adjust the tilt of the mirror to make the reflected beam leveled against the surface of the table. Install the half-wave plate (HWP) and linear polarizer (polarizer 1) after M1. The linear polarizer is used to switch the laser beam between the measurement arm and the calibration arm and ensure the polarization purity. The laser power after polarizer 1 can be tuned by adjusting the orientation of the HWP.

5 Install the PBS ~350 mm away from M1. Adjust the orientation of the PBS to make the outgoing, vertically polarized beam nearly align with the table holes. This can also be checked by looking at the weak surface-reflected beam spot at the position of polarizer 1 with a small target card.

6 Install mirrors M2 and M3 to guide the beam into the microscope body and make the beam propagate upright after mirror M4. To achieve good alignment, build an alignment assembly using cage mounts which includes two irises spaced by more than 400 mm. Ensure that the aligning assembly ends with a mounting adapter to screw the assembly onto a free slot of the objective turret. To align, first uninstall the microscope translational stage, rotate the objective turret to a free slot, and mount the aligning assembly. Adjust the beam direction to make the beam pass through the center of two irises simultaneously; this can be done by tuning the adjustment screws of the mirror mounts (two screws per mirror, which tune the horizontal and vertical tilt degrees of freedom). Once alignment is achieved, remove the aligning assembly and mount the translational stage back onto the microscope body.

▲ **CRITICAL STEP** After M4, the beam should be upright without tilt. If it is tilted, the alignment of fiber coupling in Step 9 will not work for Brillouin beam path, which will significantly affect the collection efficiency of the Brillouin signal. Before implementing the alignment assembly, it is important to ensure the two irises are coaxial on the cage mount. If not, either label the correct position on the iris far from the threading adapter or use only one iris for alignment by sliding it along the cage rods.

? TROUBLESHOOTING

7 Mount a mirror (not shown in the figures) above the translational stage with the reflective surface facing the laser beam to reflect the laser beam back along its original path. Adjust the tip/tilt of the mirror such that the reflected beam spot overlaps with the original one on M2. An iris can be used for this step within the M1–M2 beam path for ease of visual alignment. In this case, the iris is centered on the incident beam and the reflected beam spot should be adjusted to retrace back to the center of the iris.

8 Install the Brillouin filter cube in one position of filter turret 1 of the commercial microscope. Set the fast axis of the quarter-wave plate (QWP) inside to be at 45° to the polarization orientation of the beam. To achieve this, place a power meter between the PBS and objective 2 and then rotate the orientation of the QWP until the maximum power is detected.

9 Place a target card 20 cm away from the PBS and mark the center of the beam. Install objective 2. Adjust the height and tilt of objective 2 to ensure that the center of the output beam overlaps with the marker, then move the card away. Install one end of the single-mode fiber on a 3D translational stage. In case the height of the stage does not match the laser beam, install the stage on a stable post (e.g., 1.5-inch stainless steel) or a customized base. Finely adjust the position of the fiber port to achieve the maximum coupling of the laser beam, which can be monitored by using a power meter at the output end of the fiber.

▲ **CRITICAL STEP** Ensure that the axes of objective 2 (by adjusting the height and tilt) and the fiber port are aligned with the optical axis of the beam. Otherwise, the coupling efficiency could be greatly affected.

? TROUBLESHOOTING

10 Align the calibration arm (Fig. 3b). Adjust the orientation of polarizer 1 to allow a portion of the beam to pass through the PBS. Install the mirror (M5) ~120 mm away from the PBS. Set the mirror at ~45° to the incoming laser beam so that the reflected beam aligns with the table holes. Install QWP 2 and the lens ($f = 45$ mm). Set the fast axis of QWP 2 to be at 45° to the polarization orientation of the incoming beam, which can be achieved by following the same procedure used to install the Brillouin filter cube in Step 8.

Building the Brillouin spectrometer ● Timing 3–5 d

11 Identify at least 1,800 mm by 300 mm of free space on the optical table (Supplementary Fig. 2). Mount the EMCCD camera on the customized mounting stand and install the stand at one end of the free space. Attach lens pair LP to the camera window.

! CAUTION The EMCCD camera is heavy. Ensure that the mounting stand is properly fixed before installing the camera.

12 Temporarily place the fiber coupler close to the EMCCD camera. Adjust the height of the beam to be in the center of the EMCCD camera. To avoid damage to the camera under direct laser illumination, the power of the laser beam should be very low (<0.01 mW) and the camera should be set to no gain and low acquisition time (e.g., <1 ms). The parameters can be further adjusted for best visual inspection on the camera.

! CAUTION To avoid damage to the camera, the laser power should be low enough and the gain of the camera should be disabled before illumination with the laser beam.

13 Install the fiber coupler at the opposite end of the camera along the table's free space (Fig. 3b). Install and adjust mirrors M6 and M7 such that the laser beam after M7 is aligned, i.e., straight to table holes, parallel to the table height, and illuminating the center of the EMCCD camera.

14 Assemble the 4f unit (SL3, SL4: $f = 40$ mm) using the cage system mounting and fully open the aperture of iris SF, which is mounted on a 2D translational stage. Place a target card in front of the EMCCD camera and mark the position of the laser spot. Place the 4f unit far away from the target card. Adjust the distance between lenses SL3 and SL4 such that the size and position of the beam spot on the target card does not change. This can be double checked by using a commercial shear plate interferometer. Place a power meter after the 4f unit. Close the aperture of the iris to the minimum. Finely adjust the position of iris SF along the optical axis and the 2D translational stage until the output power is maximum. This ensures that the iris is on the back focal plane of lens SL3. When this is done, fully open the iris.

15 Reinstall the 4f unit immediately in front of the EMCCD camera such that the back focal plane of SL4 overlaps with the front focal plane of LP. Ensure that the position of the beam spot does not change after installation.

▲ CRITICAL STEP It is important to ensure that the 4f unit is aligned with the optical axis. To facilitate this alignment, two irises can be used to determine the beam path by temporarily attaching them to the unit before SL3 and after SL4, respectively. The beam position can be checked with the EMCCD camera.

16 Place the slit (mask 2) horizontally on a 1D translational stage. Install the stage in front of the 4f unit so that the mask is ~40 mm away from the first surface of SL3. Adjust the position of the slit along the beam path (z-axis) such that its blades are sharply imaged onto the EMCCD camera; adjust the lateral position of the slit (x–y plane) so that it is centered on the light beam.

17 Install a 1D translational stage ~200 mm away from mask 2 and make its moving axis along the optical axis (z-axis). Install lens SL2 ($f = 200$ mm) on the stage. Adjust the stage such that the back focal plane of lens SL2 is on mask 2. Install another 1D translation stage ~400 mm away from SL2 and install lens SL1 ($f = 200$ mm) on the stage. Adjust the position of SL1 to make the output beam of SL2 collimated, which can be checked using a shearing interferometer.

18 Carefully mount VIPA 2 onto the holder with the entrance AR-coated window oriented vertically (Fig. 3b). Install a 2D translation stage (a combination of two 1D stages) ~200 mm away from SL2. Install the VIPA 2 holder on the 2D stage. Set the height of VIPA 2 such that the beam spot is located close to the top of the entrance window.

19 Carefully slide VIPA 2 into the beam path such that the focused beam spot is coupled into the entrance window. Adjust the horizontal translation stage and the horizontal tilt degree of freedom of VIPA 2 to optimize the coupling, which can be monitored by using a target card after VIPA 2. Finely adjust the location of VIPA 2 along the optical axis to make the last surface of VIPA 2 overlap with the back focal plane of lens SL1. To achieve this, place a power meter at the output of VIPA 2, and repeat adjustments of VIPA 2 until the maximum power is detected.

▲ CRITICAL STEP The throughput of VIPA 2 should be optimized in this step; at least 50% should be achieved. Since the VIPA pattern is large, in case the sensor is not big enough, a positive lens with short focal length can be used to help light collection for the power meter.

? TROUBLESHOOTING

20 Finely adjust the position of lens SL2 along the optical axis until the spectral lines appear sharp on the EMCCD camera (Fig. 7a). Record the spectrum and calculate the experimental finesse of the spectrometer, which is defined as the ratio of the distance between adjacent diffraction order lines to the FWHM of one line. Aim for finesse >30.

▲ CRITICAL STEP To achieve the expected finesse, the vertical tilt degree of freedom of VIPA 2 may need slight adjustment such that the output pattern of VIPA 2 is leveled horizontally, which can be checked using a target card immediately after VIPA 2 (Supplementary Fig. 3). Practice on the adjustment of both the horizontal and vertical tilt degrees of freedom is suggested for familiarization with their functions.

? TROUBLESHOOTING

21 Slide VIPA 2 fully out of the beam path.

22 Install a 1D translational stage ~200 mm away from lens SL1 and align its moving axis with the optical axis. Assemble a vertical stage on the translation stage. Install the slit (mask 1) vertically on the vertical stage. Adjust the position of the slit such that its blades are sharply imaged onto the EMCCD camera.

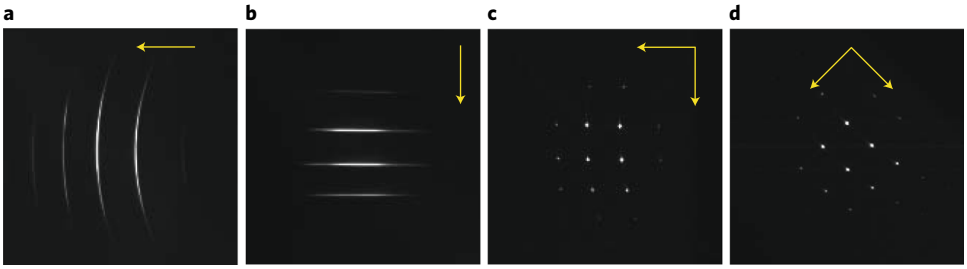

Fig. 7 | VIPA pattern of the Brillouin spectrometer. a, Dispersion pattern of VIPA 2 along horizontal axis. **b**, Dispersion pattern of VIPA 1 along vertical axis. **c**, Pattern of the combination of two VIPAs. **d**, VIPA pattern after rotating the camera by 45°. The arrows indicate the dispersion axes.

23 Install a 1D translation stage ~200 mm away from mask 1 in the same way as in the last step. Install cylindrical lens C2 on the stage such that its height axis is vertically aligned. Adjust the stage such that the back focal plane of C2 is on mask 1.

24 Install a 1D translation stage ~400 mm away from C2 in the same way as in the last step. Install cylindrical lens C1 on the stage in the same way as in the last step. Finely adjust the position of C1 such that the output beam of C2 is collimated, which can be checked using a commercial shear plate interferometer.

25 Carefully mount VIPA 1 onto the holder with the entrance window oriented horizontally and located on the top of the holder (Fig. 3b). Install a 1D translation stage ~200 mm away from C2 in the same way as in the last step. Assemble a vertical stage on the translation stage. Install VIPA 1 on the vertical stage such that the entrance window is lower than the beam.

26 Carefully raise VIPA 1 into the beam path such that the focused beam spot is coupled into the entrance window at the middle. Adjust the vertical tilt degree of freedom of VIPA 1 and the vertical stage to optimize the coupling, which can be monitored by using a target card after VIPA 1. Finely adjust the location of VIPA 1 along the optical axis to make the last surface of VIPA 1 at the back focal plane of C1. To achieve this, place a power meter at the output of VIPA 1 and repeat adjustments of VIPA 1 until the maximum power is detected.
▲ **CRITICAL STEP** The throughput of VIPA 1 should be optimized in this step; at least 50% should be achieved.

27 Finely adjust the position of CL2 along the optical axis until the spectral lines appear sharp on the EMCCD camera (Fig. 7b). Record the spectrum and calculate the finesse (as defined in Step 20). Aim for finesse >30.
▲ **CRITICAL STEP** To achieve the expected finesse, the horizontal tilt degree of freedom of VIPA 1 may need slight adjustment such that the output pattern of VIPA 1 is straight vertically, which can be checked using a target card immediately after VIPA 1. Practice with the adjustment of both the horizontal and vertical tilt degrees of freedom is suggested for familiarization with their functions.
? TROUBLESHOOTING

28 Carefully slide in VIPA 2 until observing horizontally and vertically spaced dots, which are the spectra of the single-mode laser. Tune both VIPAs to the third or fourth order by finely adjusting the tilt angle (the vertical tilt degree of freedom for VIPA 1 and the horizontal tilt degree of freedom for VIPA 2) such that the central four brightest spots are equally spaced (Fig. 7c).
! CAUTION Before implementing adjustments, ensure that the correct degree of freedom of tilting is located. Adjusting the wrong degree of freedom will distort the VIPA pattern.
? TROUBLESHOOTING

29 Slightly detach the EMCCD camera from the mounting stand by loosening the screws. Carefully rotate the camera by 45° anticlockwise such that the two dots previously in diagonal are leveled (Fig. 7d). Reattach the camera to the mounting stand by fastening the screws. This step allows the Brillouin spectrum to be dispersed along a horizontal axis on the camera, which can be helpful for image processing and binning.
! CAUTION The camera is heavy. It is strongly suggested to implement this step with a team of two people.

30 Use the construction rails and black hardboard to build an optical enclosure for the entire spectrometer. The recommended size is 70 inches (length) × 11 inches (width) × 13 inches (height). Keep one side of the enclosure open to ensure easy accessibility to the components (especially the

VIPAs and masks) in the spectrometer. Cover all the gaps between the enclosure and the table surface with black tape. Cover the enclosure with blackout fabric (9 ft × 5 ft).

▲ **CRITICAL STEP** The EMCCD is a main heat source and itself needs air cooling. To remove the effect of thermal fluctuations on the stability of the spectrometer, the EMCCD should be placed outside the enclosure. If temperature fluctuation is a concern, the temperature inside the enclosure can be monitored using a thermometer.

Optimizing the Brillouin microscope ● Timing 8–10 h

31 Close the two masks such that the laser spots just disappear. Remove the mirror installed on top of the microscope. Restore the objective turret to objective 1 (40×, 0.6 NA, Olympus). Place a Petri dish containing methanol into the sample holder.

32 Adjust the orientation of polarizer 1 to ensure that the laser power at the output of objective 1 is at least 10 mW. Enable the gain of the EMCCD camera and set the value of the gain to the maximum (i.e., 300). Set the acquisition time to 0.1 s. In case the laser spots are saturating the camera, further adjust the masks to block them.

33 Adjust the position of objective 1 such that the laser beam is focused into the sample. Finely adjust the collar of objective 1 to optimize the intensity of the Brillouin signal. Carefully adjust the 3D stage that carries the fiber port to optimize the fiber coupling. Finely adjust the location and tilt angle of the two VIPAs to further optimize the intensity of the Brillouin signal and ensure that the two Brillouin peaks have balanced intensity.

▲ **CRITICAL STEP** Since the prealignment of the fiber coupling might be imperfect, high laser power is preferred to generate a strong Brillouin signal that can be observed by the camera. Alignment of the fiber coupling without the indication of the Brillouin signal should mostly be avoided.

? TROUBLESHOOTING

34 Adjust spatial filter SF to optimize the background suppression. Place a glass-bottomed dish containing water into the sample holder. Move the focal plane of objective 1 close to the interface between the water and dish so that both the Brillouin signal of the water and the back-reflection noise appear. Slowly close the aperture of SF to suppress the background noise until observing the drop of the Brillouin signal. Slightly adjust the 2D translational mount to optimize the noise suppression while maintaining/resuming the Brillouin signal.

35 Install the apodization filters. Adjust the focal plane of objective 1 above the bottom of the dish and record the spectrum (B_{spec} 1). Then move the focal plane close to the interface between the sample and the bottom of the dish such that some background noise appeared and record the spectrum (N_{bgd} 1). Install a vertical stage immediately after VIPA 1. Install filter 1 on the stage such that its apodization edge is parallel with the entrance window of VIPA 1 (Fig. 3b). Install a horizontal stage immediately after VIPA 2. Install filter 2 on the stage such that its apodization edge is parallel with the entrance window of VIPA 2 (Fig. 3b).

▲ **CRITICAL STEP** Carefully adjust the position of filters 1 and 2 such that the background noise is largely removed while the loss of Brillouin signal is small, then record the spectrum (N_{bgd} 2). Return objective 1 to its initial position and record the spectrum again (B_{spec} 2). The suppression of background noise and loss of the Brillouin signal can then be quantified by using the recorded spectra (N_{bgd} 1, N_{bgd} 2) and (B_{spec} 1, B_{spec} 2), respectively. With both filters properly positioned, the background noise can be reduced by 10–15 dB while the loss of Brillouin signal is <10%.

36 Measure the spectral precision and SNR of the spectrometer; confirm the shot-noise-limited curve to verify the optimization of the spectrometer. To quantify the spectral precision, repeatedly take measurements of a standard sample (methanol or water) for 300 times. With an input power of 10 mW and acquisition time of 100 ms, the spectral precision should be within 10 MHz (Fig. 8a,b). In case needed, the long-term stability can be estimated by the Allen variance[134]. To verify shot-noise-limited operation, quantify the SNR of the Brillouin signal using various power levels and/or acquisition times. Plot the results for the SNR versus the input energy on a log–log scale. Under shot-noise-limited operation, the slope should be 0.5 (Fig. 8c). For SNR quantification, 300 frames are recorded at each power level, and the average and standard deviation of the peak intensity of the Brillouin signal are calculated after deducting the background. The SNR is then determined by the ratio of the average to the standard deviation.

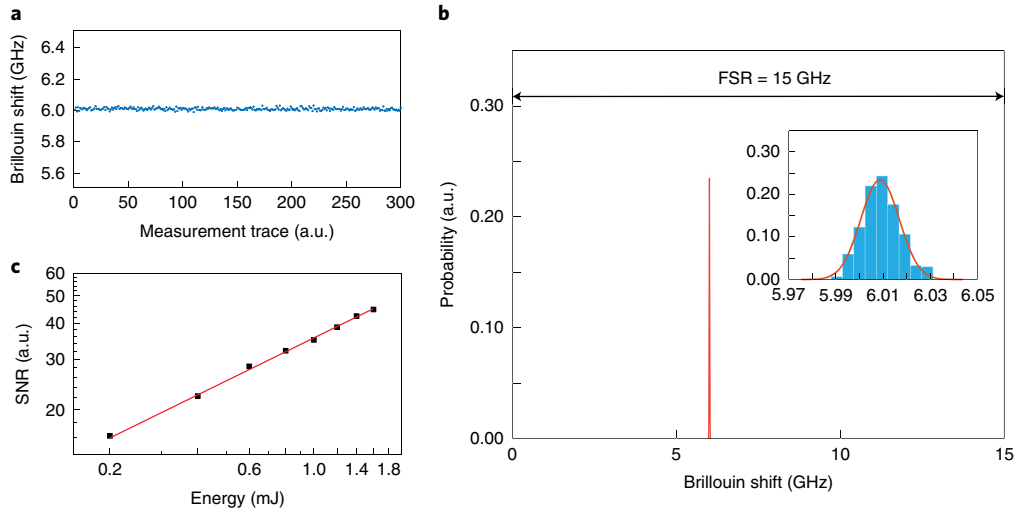

Fig. 8 | Characterization of the Brillouin spectrometer. a, Time trace of 300 times measurement of water. **b**, Histogram of the Brillouin shift precision. Inset shows a zoomed-in plot. The linewidth of the histogram is 8 MHz. **c**, Shot-noise-limited curve of water sample with laser power of 10 mW and various acquisition times. Dots are measured data, and the red curve is obtained from the linear fitting of the data on a log–log scale. The slope is 0.4934.

▲ **CRITICAL STEP** The spectral precision and the shot-noise-limited curve are key parameters to quantify the performance of the spectrometer. If the anticipated value is not achieved, Steps 11–34 should be carefully revisited.

? TROUBLESHOOTING

Preparing samples for Brillouin imaging ● Timing 1–3 days

37 Coat a glass-bottomed Petri dish with a thin hydrogel layer whenever possible[135]. Seed live cells into the dish (30,000 cells per dish for NIH 3T3 cells) in 2 ml cell culture medium and incubate them for >12 h to ensure cells are well attached on the substrate. If needed, stain the cells with fluorescent dyes according to the manufacturer's instructions.

▲ **CRITICAL STEP** Preparation of cellular samples may need to be optimized/adjusted depending on the cell line and the specific biological question to be addressed.

Imaging the sample using the Brillouin microscope ● Timing 1–8 h

38 Initialize the Brillouin spectrometer. Place a dish containing standard material (e.g., water) on the sample stage. Adjust the orders and coupling of the VIPAs such that the intensities of two Brillouin peaks are optimized and roughly equaled. Adjust the position of two masks such that the laser peaks are properly blocked. Adjust the focal plane of objective 1 close to the interface between the water and glass such that some amount of background noise appears in the spectrum. Carefully adjust the position of the two filters to suppress the noise.

▲ **CRITICAL STEP** Due to drift of the laser frequency or the mechanical components, the Brillouin spectrometer should be optimized from day to day. This routine maintenance ensures that high-quality data can be obtained in the experiment.

? TROUBLESHOOTING

39 Calibrate the Brillouin spectrometer. Use the calibration arm of the spectrometer (Fig. 3b) to record the Brillouin signals of two standard materials (e.g., water and methanol). Repeatedly record the signal of each material for at least 300 times.

▲ **CRITICAL STEP** The calibration ensures that the experimental data are not affected by instrumental drift, thus making the results obtained on different days comparable. Hence, the calibration process should be implemented whenever instrumental drift is a concern; For example, when the Brillouin peak has shifted by as much as 1 pixel over time or the intensities of the two peaks are distinctly unbalanced (ratio <50%), recalibration should be implemented after recovering the Brillouin signal by adjusting the two VIPAs.

40 Place the dish containing the sample from Step 37 onto the stage. Switch to the bright-field or fluorescent channel by rotating the turret (filter turret 1) that carries the Brillouin filter cube. Adjust the 2D stage and the focus of objective 1 to locate the sample of interest. Record the bright-field/fluorescent image using the CMOS camera. Switch back to the Brillouin channel. Adjust the laser power to ensure that the Brillouin signal of the sample is strong enough (e.g., peak intensity >10,000 counts under EM gain).

41 Set up the scanning strategy. Use the raster scanning mode for 2D mapping. Based on the location and size of the sample, determine the scanning region, step size, scanning plane, and acquisition time. Save the scanning information for future use in data postprocessing.

42 Start the data acquisition from the sample by raster scanning. A straightforward home-built LabVIEW program can automatically save the Brillouin spectrum at each point.

43 Repeat Steps 40–42 until all the samples have been measured.
? TROUBLESHOOTING

44 Recalibrate the Brillouin spectrometer using standard materials according to Step 39 before finishing the experiments.

Data postprocessing ● Timing 1–8 h

45 Calculate the calibration parameters FSR and PR. Load the data file of the calibration from Steps 39 and 44. Fit the spectrum of each sampling point using a Lorentzian function to extract the peak distance using the MATLAB program. Use equation (3) to calculate the corresponding FSR and PR with known Brillouin shifts of standard materials (for a 660-nm laser source, $\nu_w = 6.01$ GHz and $\nu_m = 4.49$ GHz). The average of all the samplings can be used as the value of FSR and PR for retrieving the Brillouin shift of the sample. Example MATLAB codes are provided in Supplementary Data 1.

46 Retrieve the Brillouin shift of the sample. Load the data file of the measurement. First interpolate then fit the spectrum of each pixel using a Lorentzian function to extract the peak distance using the MATLAB program. Use the calibrated values of FSR and PR to retrieve the Brillouin shift at each pixel. Save the results into a 1D vector. If there is more than one sample, repeat this step until all the samples have been processed. Example MATLAB codes are provided in Supplementary Data 1.

47 Reconstruct the 2D Brillouin image of the sample. In case the data are collected by raster scanning, use the 'reshape' function in MATLAB to convert the 1D vector of Brillouin shifts from the last step into a 2D Brillouin image.

48 Analyze the mechanical properties of the sample. Extract the Brillouin image of the entire sample or its subregion by coregistering the 2D Brillouin image with the corresponding bright-field or fluorescent image. Use the averaged Brillouin shift of the selected region to represent the mechanical property.

Troubleshooting

Troubleshooting advice can be found in Table 1.

Table 1 | Troubleshooting table

Step	Problem	Possible reason	Solution
6	Beam after M4 is straight but not in the center of the iris	Position of M3 is not correct	Carefully shift M3 along the optical axis without changing the reflection angle. Observe the position of the beam spot. Repeat this process until the beam passes through the center of both irises
9	No light detected at the output port	Coupling of the fiber is poor	Check the beam quality in front of the back focal plane of objective 2 to ensure that there is no beam clipping or distortion. Increase the laser power until observing laser light at the output port of the fiber. Then adjust the 3D stage to optimize the coupling. In case no signal is observed at maximum laser power, start over this step to ensure that the beam position was not altered after installing objective 2
19	No light at the output of the VIPA	The tilt angle of the VIPA is too small or the beam is not on the entrance window	Increase the tilt angle of the VIPA to ensure that the reflection angle of the incoming focused beam is large enough to be coupled into the VIPA's cavity. Meanwhile, carefully adjust the horizontal translation stage to ensure that the beam is on the entrance window

Table continued

Table 1 (continued)

Step	Problem	Possible reason	Solution
20	Spectral line is not leveled or sharp	Vertical tilt degree of freedom of the VIPA is misaligned	Place a target card at the output of the VIPA to check if the pattern is tilted. If so, adjust the vertical tilt degree of freedom of the VIPA to make them aligned. Good alignment will ensure a sharp pattern at the focal plane of lens SL2
27	Spectral line is not straight or sharp	Horizontal tilt degree of freedom of the VIPA is misaligned	Use the same solution as for Step 20
28	Spectral dots are not circular	SL2 is slightly misaligned	Slide VIPA 1 out of the path and readjust the position of SL2 such that the pattern of VIPA 2 is sharp. Then slide in VIPA 1 to get spectral dots. If it is still not circular, slightly adjust the position of C2
33	No Brillouin signal is observed	Position of the fiber port is misaligned	Increase the laser power and the acquisition time of the EMCCD camera until a Brillouin signal can be observed. Then adjust the 3D stage to optimize the signal
	Background noise is too high	Back-reflection from optical component	Move away the sample dish. If noise disappears, clean the bottom of the dish, or change to a new dish. If not, check if there is any back-reflection from optical components on either the measurement or collection arm. This can be implemented by using a dark paper card to block the beam path of each component sequentially. Once the component has been located, slightly tilt it to remove the back-reflection
36	Result is not shot-noise limited	Stray light from ambient or sample	Adjust the focal plane of objective 1 far away from the interface to avoid any reflection light. Carefully check the optical enclosure to ensure that there is no stray light from the ambient environment
38	Brillouin peaks show quick shifting	Frequency of the laser is drifting abnormally	Ensure that the room temperature is 20–25 °C and stable. Avoid placing the laser close to the vent of the room. Ensure that the laser is fully warmed up before the experiment (>30 min at least). Check the temperature of the laser head to ensure that it is properly cooled
43	Brillouin peaks show slow shifting over time	Frequency of the laser is drifting normally	More frequent calibrations should be implemented. Follow the guideline regarding periodical calibration in section 'Brillouin spectrum and calibration'

Timing

Steps 1–10, setting up the microscope and add-on optics: 2–4 d
Steps 11–30, building the Brillouin spectrometer: 3–5 d
Steps 31–36, optimizing the Brillouin microscope: 8–10 h
Step 37, preparing samples for Brillouin imaging: 1–3 d
Steps 38–44, imaging the sample using the Brillouin microscope: 1–8 h
Steps 45–48, data postprocessing: 1–8 h

Anticipated results

Figure 9 shows typical Brillouin images of live 3T3 cells in both control and treated condition. The coregistration of the Brillouin image and the bright-field/fluorescent image can be implemented in either ImageJ or MATLAB. As the Brillouin image usually has lower resolution than the bright-field/fluorescent image, the latter needs to be resized to match the former before coregistration. The subcellular regions can then be outlined by overlaying two images. With the coregistered bright-field/fluorescent image (Fig. 9a,b, left panels), Brillouin shifts of subcellular regions (that is, cytoplasm and nucleus) can be extracted and quantified (Fig. 9c). Generally, the nucleus has a higher Brillouin shift than the cytoplasm. After treatment with cytochalasin D, which is used to depolymerize the actin filament, the Brillouin shift of both the cytoplasm and nucleus decreases.

Reporting Summary

Further information on research design is available in the Nature Research Reporting Summary linked to this article.

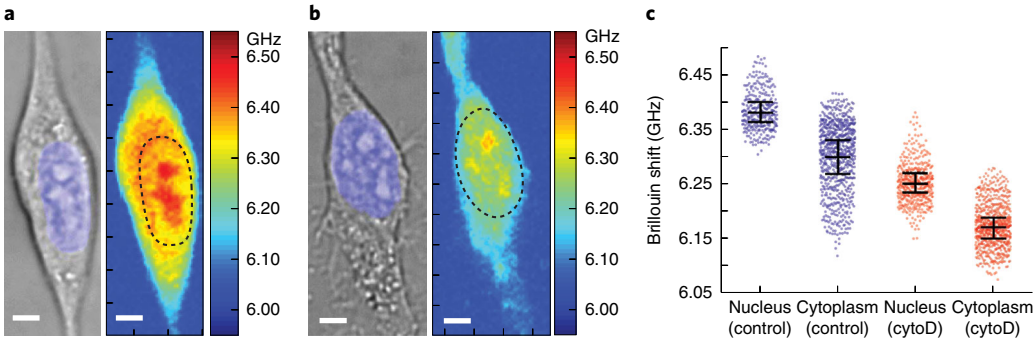

Fig. 9 | Brillouin image of live 3T3 cells. a, Cell in control condition. **b**, Cell with treatment by actin depolymerization drug (cytochalasin D). In each subfigure, the left and right panel show the bright-field/fluorescent image and Brillouin image, respectively. The blue shadow and dashed curves indicate the nucleus. Scale bar 5 μm. **c**, Brillouin shifts of subcellular regions (that is, nucleus and cytoplasm) of both control and treated cells. Dots represent pixels, and values represent the mean ± standard deviation.

Data availability

The authors declare that all data supporting the findings of this study are available within the paper and its Supplementary Information files. The raw Brillouin spectra of Figs. 8 and 9 are available via Figshare (https://figshare.com/articles/dataset/raw_data_to_Fig_8_9/13135760). Source data are provided with this paper.

Code availability

The MATLAB code to analyze images as well as representative raw data are provided as Supplementary Data 1.

References

1. Vogel, V. & Sheetz, M. Local force and geometry sensing regulate cell functions. *Nat. Rev. Mol. Cell Biol.* **7**, 265–275 (2006).
2. Discher, D. E., Janmey, P. & Wang, Y.-L. Tissue cells feel and respond to the stiffness of their substrate. *Science* **310**, 1139–1143 (2005).
3. Wozniak, M. A. & Chen, C. S. Mechanotransduction in development: a growing role for contractility. *Nat. Rev. Mol. Cell Biol.* **10**, 34–43 (2009).
4. Miller, C. J. & Davidson, L. A. The interplay between cell signalling and mechanics in developmental processes. *Nat. Rev. Genet.* **14**, 733–744 (2013).
5. Gilkes, D. M., Semenza, G. L. & Wirtz, D. Hypoxia and the extracellular matrix: drivers of tumour metastasis. *Nat. Rev. Cancer* **14**, 430–439 (2014).
6. Orr, A. W., Helmke, B. P., Blackman, B. R. & Schwartz, M. A. Mechanisms of mechanotransduction. *Dev. Cell* **10**, 11–20 (2006).
7. Polacheck, W. J. & Chen, C. S. Measuring cell-generated forces: a guide to the available tools. *Nat. Methods* **13**, 415–423 (2016).
8. Bao, G. & Suresh, S. Cell and molecular mechanics of biological materials. *Nat. Mater.* **2**, 715–725 (2003).
9. Campas, O. A toolbox to explore the mechanics of living embryonic tissues. *Semin. Cell Dev. Biol.* **55**, 119–130 (2016).
10. Heinisch, J. J., Dupres, V., Alsteens, D. & Dufrêne, Y. F. Measurement of the mechanical behavior of yeast membrane sensors using single-molecule atomic force microscopy. *Nat. Protoc.* **5**, 670 (2010).
11. Stewart, M. P., Toyoda, Y., Hyman, A. A. & Müller, D. J. Tracking mechanics and volume of globular cells with atomic force microscopy using a constant-height clamp. *Nat. Protoc.* **7**, 143 (2012).
12. Benaglia, S., Gisbert, V. G., Perrino, A. P., Amo, C. A. & Garcia, R. Fast and high-resolution mapping of elastic properties of biomolecules and polymers with bimodal AFM. *Nat. Protoc.* **13**, 2890–2907 (2018).
13. Efremov, Y. M., Cartagena-Rivera, A. X., Athamneh, A. I., Suter, D. M. & Raman, A. Mapping heterogeneity of cellular mechanics by multi-harmonic atomic force microscopy. *Nat. Protoc.* **13**, 2200–2216 (2018).
14. Krieg, M. et al. Atomic force microscopy-based mechanobiology. *Nat. Rev. Phys.* **1**, 41–57 (2019).
15. Trier, S. M. & Davidson, L. A. Quantitative microscopy and imaging tools for the mechanical analysis of morphogenesis. *Curr. Opin. Genet. Dev.* **21**, 664–670 (2011).
16. Chevalier, N. R., Gazguez, E., Dufour, S. & Fleury, V. Measuring the micromechanical properties of embryonic tissues. *Methods* **94**, 120–128 (2016).
17. Evans, E. & Yeung, A. Apparent viscosity and cortical tension of blood granulocytes determined by micropipet aspiration. *Biophys. J.* **56**, 151–160 (1989).
18. Hochmuth, R. M. Micropipette aspiration of living cells. *J. Biomech.* **33**, 15–22 (2000).

19. Desprat, N., Guiroy, A. & Asnacios, A. Microplates-based rheometer for a single living cell. *Rev. Sci. Instrum.* **77**, 055111 (2006).
20. Caille, N., Tardy, Y. & Meister, J.-J. Assessment of strain field in endothelial cells subjected to uniaxial deformation of their substrate. *Ann. Biomed. Eng.* **26**, 409–416 (1998).
21. Svoboda, K. & Block, S. M. Biological applications of optical forces. *Annu. Rev. Biophys. Biomol. Struct.* **23**, 247–285 (1994).
22. Lee, W. M., Reece, P. J., Marchington, R. F., Metzger, N. K. & Dholakia, K. Construction and calibration of an optical trap on a fluorescence optical microscope. *Nat. Protoc.* **2**, 3226 (2007).
23. Wang, N., Butler, J. P. & Ingber, D. E. Mechanotransduction across the cell surface and through the cytoskeleton. *Science* **260**, 1124–1127 (1993).
24. Zhang, Y. et al. Interfacing 3D magnetic twisting cytometry with confocal fluorescence microscopy to image force responses in living cells. *Nat. Protoc.* **12**, 1437 (2017).
25. Bausch, A. R., Möller, W. & Sackmann, E. Measurement of local viscoelasticity and forces in living cells by magnetic tweezers. *Biophys. J.* **76**, 573–579 (1999).
26. Mason, T., Ganesan, K., Van Zanten, J., Wirtz, D. & Kuo, S. C. Particle tracking microrheology of complex fluids. *Phys. Rev. Lett.* **79**, 3282 (1997).
27. Serwane, F. et al. In vivo quantification of spatially varying mechanical properties in developing tissues. *Nat. Methods* **14**, 181–186 (2017).
28. Guck, J. et al. The optical stretcher: a novel laser tool to micromanipulate cells. *Biophys. J.* **81**, 767–784 (2001).
29. Wang, S. & Larin, K. V. Optical coherence elastography for tissue characterization: a review. *J. Biophotonics* **8**, 279–302 (2015).
30. Kennedy, B. F., Wijesinghe, P. & Sampson, D. D. The emergence of optical elastography in biomedicine. *Nat. Photonics* **11**, 215–221 (2017).
31. Gossett, D. R. et al. Hydrodynamic stretching of single cells for large population mechanical phenotyping. *Proc. Natl Acad. Sci. USA* **109**, 7630–7635 (2012).
32. Otto, O. et al. Real-time deformability cytometry: on-the-fly cell mechanical phenotyping. *Nat. Methods* **12**, 199–202 (2015).
33. Hartono, D. et al. On-chip measurements of cell compressibility via acoustic radiation. *Lab Chip* **11**, 4072–4080 (2011).
34. Kang, J. H. et al. Noninvasive monitoring of single-cell mechanics by acoustic scattering. *Nat. Methods* **16**, 263–269 (2019).
35. Dil, J. G. Brillouin scattering in condensed matter. *Rep. Prog. Phys.* **45**, 285–334 (1982).
36. Scarcelli, G. & Yun, S. H. Confocal Brillouin microscopy for three-dimensional mechanical imaging. *Nat. Photonics* **2**, 39–43 (2008).
37. Prevedel, R., Diz-Muñoz, A., Ruocco, G. & Antonacci, G. Brillouin microscopy: an emerging tool for mechanobiology. *Nat. Methods* **16**, 969–977 (2019).
38. Palombo, F. & Fioretto, D. Brillouin light scattering: applications in biomedical sciences. *Chem. Rev.* **119**, 7833–7847 (2019).
39. Scarcelli, G. et al. Noncontact three-dimensional mapping of intracellular hydro-mechanical properties by Brillouin microscopy. *Nat. Methods* **12**, 1132–1134 (2015).
40. Scarcelli, G., Kim, P. & Yun, S. H. In vivo measurement of age-related stiffening in the crystalline lens by Brillouin optical microscopy. *Biophys. J.* **101**, 1539–1545 (2011).
41. Scarcelli, G., Pineda, R. & Yun, S. H. Brillouin optical microscopy for corneal biomechanics. *Investig. Ophthalmol. Vis. Sci.* **53**, 185–190 (2012).
42. Scarcelli, G., Besner, S., Pineda, R. & Yun, S. H. Biomechanical characterization of keratoconus corneas ex vivo with Brillouin microscopy. *Investig. Ophthalmol. Vis. Sci.* **55**, 4490–4495 (2014).
43. Scarcelli, G., Besner, S., Pineda, R., Kalout, P. & Yun, S. H. In vivo biomechanical mapping of normal and keratoconus corneas. *JAMA Ophthalmol.* **133**, 480–482 (2015).
44. Elsayad, K. et al. Mapping the subcellular mechanical properties of live cells in tissues with fluorescence emission-Brillouin imaging. *Sci. Signal* **9**, rs5 (2016).
45. Schlüßler, R. et al. Mechanical mapping of spinal cord growth and repair in living zebrafish larvae by brillouin imaging. *Biophys. J.* **115**, 911–923 (2018).
46. Zhang, J. et al. Tissue biomechanics during cranial neural tube closure measured by Brillouin microscopy and optical coherence tomography. *Birth Defects Res.* **111**, 991–998 (2018).
47. Antonacci, G., de Turris, V., Rosa, A. & Ruocco, G. Background-deflection Brillouin microscopy reveals altered biomechanics of intracellular stress granules by ALS protein FUS. *Commun. Biol.* **1**, 1–8 (2018).
48. Gouveia, R. M. et al. Assessment of corneal substrate biomechanics and its effect on epithelial stem cell maintenance and differentiation. *Nat. Commun.* **10**, 1496 (2019).
49. Margueritat, J. et al. High-frequency mechanical properties of tumors measured by Brillouin light scattering. *Phys. Rev. Lett.* **122**, 018101 (2019).
50. Conrad, C., Gray, K. M., Stroka, K. M., Rizvi, I. & Scarcelli, G. Mechanical characterization of 3D ovarian cancer nodules using Brillouin confocal microscopy. *Cell. Mol. Bioeng.* **12**, 215–226 (2019).
51. Zhang, J. et al. Nuclear mechanics within intact cells is regulated by cytoskeletal network and internal nanostructures. *Small* **16**, 1907688 (2020).
52. Lindsay, S., Anderson, M. & Sandercock, J. Construction and alignment of a high performance multipass vernier tandem Fabry–Perot interferometer. *Rev. Sci. Instrum.* **52**, 1478–1486 (1981).

53. Hickman, G. D. et al. Aircraft laser sensing of sound velocity in water: Brillouin scattering. *Remote Sens. Environ.* **36**, 165–178 (1991).
54. Harley, R., James, D., Miller, A. & White, J. Phonons and the elastic moduli of collagen and muscle. *Nature* **267**, 285–287 (1977).
55. Cusack, S. & Miller, A. Determination of the elastic constants of collagen by Brillouin light scattering. *J. Mol. Biol.* **135**, 39–51 (1979).
56. Randall, J. T. & Vaughan, J. M. Brillouin scattering in systems of biological significance. *Philos. Trans. R. Soc. Lond. A* **293**, 341–348 (1979).
57. Vaughan, J. & Randall, J. Brillouin scattering, density and elastic properties of the lens and cornea of the eye. *Nature* **284**, 489–491 (1980).
58. Randall, J. & Vaughan, J. The measurement and interpretation of Brillouin scattering in the lens of the eye. *Proc. R. Sci. Lond. B* **214**, 449–470 (1982).
59. Lee, S. et al. A Brillouin scattering study of the hydration of Li-and Na-DNA films. *Biopolymers* **26**, 1637–1665 (1987).
60. Lees, S., Tao, N.-J. & Lindsay, S. Studies of compact hard tissues and collagen by means of Brillouin light scattering. *Connect. Tissue Res.* **24**, 187–205 (1990).
61. Itoh, S.-i, Yamana, T. & Kojima, S. Quick measurement of Brillouin spectra of glass-forming material trimethylene glycol by angular dispersion-type Fabry–Perot interferometer system. *Jpn. J. Appl. Phys.* **35**, 2879 (1996).
62. Koski, K. & Yarger, J. Brillouin imaging. *Appl. Phys. Lett.* **87**, 061903 (2005).
63. Shirasaki, M. Large angular dispersion by a virtually imaged phased array and its application to a wavelength demultiplexer. *Opt. Lett.* **21**, 366–368 (1996).
64. Scarcelli, G. & Yun, S. H. Multistage VIPA etalons for high-extinction parallel Brillouin spectroscopy. *Opt. Express* **19**, 10913–10922 (2011).
65. Berghaus, K. V., Yun, S. H. & Scarcelli, G. High speed sub-GHz spectrometer for Brillouin scattering analysis. *J. Vis. Exp.* **106**, e53468 (2015).
66. Antonacci, G., Lepert, G., Paterson, C. & Török, P. Elastic suppression in Brillouin imaging by destructive interference. *Appl. Phys. Lett.* **107**, 061102 (2015).
67. Meng, Z., Traverso, A. J. & Yakovlev, V. V. Background clean-up in Brillouin microspectroscopy of scattering medium. *Opt. Express* **22**, 5410–5415 (2014).
68. Fiore, A., Zhang, J., Shao, P., Yun, S. H. & Scarcelli, G. High-extinction virtually imaged phased array-based Brillouin spectroscopy of turbid biological media. *Appl. Phys. Lett.* **108**, 203701 (2016).
69. Edrei, E., Gather, M. C. & Scarcelli, G. Integration of spectral coronagraphy within VIPA-based spectrometers for high extinction Brillouin imaging. *Opt. Express* **25**, 6895–6903 (2017).
70. Nikolić, M. & Scarcelli, G. Long-term Brillouin imaging of live cells with reduced absorption-mediated damage at 660nm wavelength. *Biomed. Opt. Express* **10**, 1567–1580 (2019).
71. Zhang, J., Fiore, A., Yun, S.-H., Kim, H. & Scarcelli, G. Line-scanning Brillouin microscopy for rapid non-invasive mechanical imaging. *Sci. Rep.* **6**, 35398 (2016).
72. Raghunathan, R. et al. Evaluating biomechanical properties of murine embryos using Brillouin microscopy and optical coherence tomography. *J. Biomed. Opt.* **22**, 086013 (2017).
73. Roberts C. J. Biomechanics in keratoconus. in *Textbook of Keratoconus: New Insights* (ed. Barbara, A.) 29–32 (Jaypee Brothers Medical Publishers, 2012).
74. Yun, S. H. & Chernyak, D. Brillouin microscopy: assessing ocular tissue biomechanics. *Curr. Opin. Ophthalmol.* **29**, 299 (2018).
75. Webb, J. N., Zhang, H., Roy, A. S., Randleman, J. B. & Scarcelli, G. Detecting mechanical anisotropy of the cornea using Brillouin microscopy. *Transl. Vis. Sci. Technol.* **9**, 26–26 (2020).
76. Eltony, A. M., Shao, P. & Yun, S.-H. Measuring mechanical anisotropy of the cornea with Brillouin microscopy. Preprint at https://arxiv.org/abs/2003.04344 (2020).
77. Shao, P. et al. Spatially-resolved Brillouin spectroscopy reveals biomechanical abnormalities in mild to advanced keratoconus in vivo. *Sci. Rep.* **9**, 1–12 (2019).
78. Reiß, S., Burau, G., Stachs, O., Guthoff, R. & Stolz, H. Spatially resolved Brillouin spectroscopy to determine the rheological properties of the eye lens. *Biomed. Opt. Express* **2**, 2144–2159 (2011).
79. Besner, S., Scarcelli, G., Pineda, R. & Yun, S.-H. In vivo Brillouin analysis of the aging crystalline lens. *Investig. Ophthalmol. Vis. Sci.* **57**, 5093–5100 (2016).
80. Weber, I. P., Yun, S. H., Scarcelli, G. & Franze, K. The role of cell body density in ruminant retina mechanics assessed by atomic force and Brillouin microscopy. *Phys. Biol.* **14**, 065006 (2017).
81. Shawky, J. H. & Davidson, L. A. Tissue mechanics and adhesion during embryo development. *Dev. Biol.* **401**, 152–164 (2015).
82. Bevilacqua, C., Sánchez-Iranzo, H., Richter, D., Diz-Muñoz, A. & Prevedel, R. Imaging mechanical properties of sub-micron ECM in live zebrafish using Brillouin microscopy. *Biomed. Opt. Express* **10**, 1420–1431 (2019).
83. Wang, N., Tytell, J. D. & Ingber, D. E. Mechanotransduction at a distance: mechanically coupling the extracellular matrix with the nucleus. *Nat. Rev. Mol. Cell Biol.* **10**, 75–82 (2009).
84. Kirby, T. J. & Lammerding, J. Emerging views of the nucleus as a cellular mechanosensor. *Nat. Cell Biol.* **20**, 373–381 (2018).
85. Meng, Z., Bustamante Lopez, S. C., Meissner, K. E. & Yakovlev, V. V. Subcellular measurements of mechanical and chemical properties using dual Raman–Brillouin microspectroscopy. *J. Biophotonics* **9**, 201–207 (2016).

86. Antonacci, G. & Braakman, S. Biomechanics of subcellular structures by non-invasive Brillouin microscopy. *Sci. Rep.* **6**, 37217 (2016).
87. Altartouri, B. et al. Pectin chemistry and cellulose crystallinity govern pavement cell morphogenesis in a multi-step mechanism. *Plant Physiol.* **181**, 127–141 (2019).
88. Zhang, J., Nou, X. A., Kim, H. & Scarcelli, G. Brillouin flow cytometry for label-free mechanical phenotyping of the nucleus. *Lab Chip* **17**, 663–670 (2017).
89. Suresh, S. Biomechanics and biophysics of cancer cells. *Acta Mater.* **55**, 3989–4014 (2007).
90. Guck, J. et al. Optical deformability as an inherent cell marker for testing malignant transformation and metastatic competence. *Biophys. J.* **88**, 3689–3698 (2005).
91. Cross, S. E., Jin, Y.-S., Rao, J. & Gimzewski, J. K. Nanomechanical analysis of cells from cancer patients. *Nat. Nanotechnol.* **2**, 780 (2007).
92. Li, Q., Lee, G. Y., Ong, C. N. & Lim, C. T. AFM indentation study of breast cancer cells. *Biochem. Biophys. Res. Commun.* **374**, 609–613 (2008).
93. Plodinec, M. et al. The nanomechanical signature of breast cancer. *Nat. Nanotechnol.* **7**, 757–765 (2012).
94. Prabhune, M., Belge, G., Dotzauer, A., Bullerdiek, J. & Radmacher, M. Comparison of mechanical properties of normal and malignant thyroid cells. *Micron* **43**, 1267–1272 (2012).
95. Wisniewski, E. et al. Dorsoventral polarity directs cell responses to migration track geometries. *Sci. Adv.* **6**, eaba6505 (2020).
96. Koski, K. J., Akhenblit, P., McKiernan, K. & Yarger, J. L. Non-invasive determination of the complete elastic moduli of spider silks. *Nat. Mater.* **12**, 262–267 (2013).
97. Mercatelli, R. et al. Morpho-mechanics of human collagen superstructures revealed by all-optical correlative micro-spectroscopies. *Commun. Biol.* **2**, 1–10 (2019).
98. Palombo, F. et al. Biomechanics of fibrous proteins of the extracellular matrix studied by Brillouin scattering. *J. R. Soc. Interface* **11**, 20140739 (2014).
99. Speziale, S. et al. Sound velocity and elasticity of tetragonal lysozyme crystals by Brillouin spectroscopy. *Biophys. J.* **85**, 3202–3213 (2003).
100. Yan, K. et al. Electrical programming of soft matter: using temporally varying electrical inputs to spatially control self assembly. *Biomacromolecules* **19**, 364–373 (2018).
101. Meng, Z. et al. Assessment of local heterogeneity in mechanical properties of nanostructured hydrogel networks. *ACS Nano* **11**, 7690–7696 (2017).
102. Bailey, M. et al. Brillouin microspectroscopy data of tissue-mimicking gelatin hydrogels. *Data Brief.* **29**, 105267 (2020).
103. Antonacci, G. et al. Quantification of plaque stiffness by Brillouin microscopy in experimental thin cap fibroatheroma. *J. R. Soc. Interface* **12**, 20150843 (2015).
104. Steelman, Z., Meng, Z., Traverso, A. J. & Yakovlev, V. V. Brillouin spectroscopy as a new method of screening for increased CSF total protein during bacterial meningitis. *J. Biophotonics* **8**, 408–414 (2015).
105. Mattana, S., Caponi, S., Tamagnini, F., Fioretto, D. & Palombo, F. Viscoelasticity of amyloid plaques in transgenic mouse brain studied by Brillouin microspectroscopy and correlative Raman analysis. *J. Innov. Opt. Health Sci.* **10**, 1742001 (2017).
106. Palombo, F. et al. Hyperspectral analysis applied to micro-Brillouin maps of amyloid-beta plaques in Alzheimer's disease brains. *Analyst* **143**, 6095–6102 (2018).
107. Troyanova-Wood, M., Gobbell, C., Meng, Z., Gashev, A. A. & Yakovlev, V. V. Optical assessment of changes in mechanical and chemical properties of adipose tissue in diet-induced obese rats. *J. Biophotonics* **10**, 1694–1702 (2017).
108. Troyanova-Wood, M., Meng, Z. & Yakovlev, V. V. Differentiating melanoma and healthy tissues based on elasticity-specific Brillouin microspectroscopy. *Biomed. Opt. Express* **10**, 1774–1781 (2019).
109. Lainović, T. et al. Micromechanical imaging of dentin with Brillouin microscopy. *Acta Biomater.* **105**, 214–222 (2020).
110. Stephen, M. A., Krainak, M. A. & Fahey, M. E. Lateral-transfer recirculating etalon spectrometer. *Opt. Express* **23**, 30020–30027 (2015).
111. Scarponi, F. et al. High-performance versatile setup for simultaneous Brillouin–Raman microspectroscopy. *Phys. Rev. X* **7**, 031015 (2017).
112. Mattana, S. et al. Non-contact mechanical and chemical analysis of single living cells by microspectroscopic techniques. *Light Sci. Appl.* **7**, 17139–17139 (2018).
113. Schneider, D. et al. Nonlinear control of high-frequency phonons in spider silk. *Nat. Mater.* **15**, 1079–1083 (2016).
114. Boyd, R. W. *Nonlinear Optics* (Academic Press, 2003).
115. Ballmann, C. W. et al. Stimulated Brillouin scattering microscopic imaging. *Sci. Rep.* **5**, 18139 (2015).
116. Remer, I. & Bilenca, A. Background-free Brillouin spectroscopy in scattering media at 780 nm via stimulated Brillouin scattering. *Opt. Lett.* **41**, 926–929 (2016).
117. Remer, I. & Bilenca, A. High-speed stimulated Brillouin scattering spectroscopy at 780 nm. *Appl. Photonics* **1**, 061301 (2016).
118. Remer, I., Shemsesh, N., Ben-Zvi, A. & Bilenca, A. High sensitivity and specificity biomechanical imaging by stimulated Brillouin scattering microscopy. *Nat. Methods* **17**, 913–916 (2020).
119. Nelson, K. A., Miller, R. D., Lutz, D. & Fayer, M. Optical generation of tunable ultrasonic waves. *J. Appl. Phys.* **53**, 1144–1149 (1982).

120. Ballmann, C. W., Meng, Z., Traverso, A. J., Scully, M. O. & Yakovlev, V. V. Impulsive Brillouin microscopy. *Optica* **4**, 124–128 (2017).
121. Krug, B., Koukourakis, N. & Czarske, J. W. Impulsive stimulated Brillouin microscopy for non-contact, fast mechanical investigations of hydrogels. *Opt. Express* **27**, 26910–26923 (2019).
122. Guo, M. et al. Cell volume change through water efflux impacts cell stiffness and stem cell fate. *Proc. Natl Acad. Sci. USA* **114**, E8618–E8627 (2017).
123. Wu, P.-J. et al. Water content, not stiffness, dominates Brillouin spectroscopy measurements in hydrated materials. *Nat. Methods* **15**, 561 (2018).
124. Scarcelli, G. & Yun, S. H. Reply to 'Water content, not stiffness, dominates Brillouin spectroscopy measurements in hydrated materials'. *Nat. Methods* **15**, 562 (2018).
125. Xiao, S., Weiner, A. M. & Lin, C. A dispersion law for virtually imaged phased-array spectral dispersers based on paraxial wave theory. *IEEE J. Quantum Electron.* **40**, 420–426 (2004).
126. Fiore, A., Bevilacqua, C. & Scarcelli, G. Direct three-dimensional measurement of refractive index via dual photon-phonon scattering. *Phys. Rev. Lett.* **122**, 103901 (2019).
127. Caponi, S., Fioretto, D. & Mattarelli, M. On the actual spatial resolution of Brillouin Imaging. *Opt. Lett.* **45**, 1063–1066 (2020).
128. Jacques, S. L. Optical properties of biological tissues: a review. *Phys. Med. Biol.* **58**, R37 (2013).
129. Scarcelli, G. & Yun, S. H. In vivo Brillouin optical microscopy of the human eye. *Opt. Express* **20**, 9197–9202 (2012).
130. Shao, P. et al. Effects of corneal hydration on brillouin microscopy in vivo. *Investig. Ophthalmol. Vis. Sci.* **59**, 3020–3027 (2018).
131. Akilbekova, D. et al. Brillouin spectroscopy and radiography for assessment of viscoelastic and regenerative properties of mammalian bones. *J. Biomed. Opt.* **23**, 097004 (2018).
132. Cardinali, M. et al. Brillouin micro-spectroscopy of subchondral, trabecular bone and articular cartilage of the human femoral head. *Biomed. Opt. Express* **10**, 2606–2611 (2019).
133. Antonacci, G., Foreman, M. R., Paterson, C. & Török, P. Spectral broadening in Brillouin imaging. *Apply. Phys. Lett.* **103**, 221105 (2013).
134. Ballmann, C. W., Meng, Z. & Yakovlev, V. V. Nonlinear Brillouin spectroscopy: what makes it a better tool for biological viscoelastic measurements. *Biomed. Opt. Express* **10**, 1750–1759 (2019).
135. Caliari, S. R. & Burdick, J. A. A practical guide to hydrogels for cell culture. *Nat. Methods* **13**, 405–414 (2016).

Acknowledgements

The authors thank M. Nikolic and A. Fiore for helpful discussions, and H. Zhang and E. Frank for helping with the LabVIEW program. This work was supported in part by the National Institutes of Health (K25HD097288, R33CA204582, U01CA202177, R01EY028666 and R01HD095520) and the National Science Foundation (CMMI 1929412 and DBI 1942003).

Author contributions

Both authors conceived the idea; J.Z. performed the experiments; both authors wrote the manuscript.

Competing interests

G.S holds patents related to Brillouin technology (US7898656B2, US8115919B2 and US20200278250A1) and is a consultant for Intelon Optics. The other authors declare no competing interests.

Additional information

Supplementary information is available for this paper at https://doi.org/10.1038/s41596-020-00457-2.

Correspondence and requests for materials should be addressed to J.Z. or G.S.

Peer review information *Nature Protocols* thanks Robert Prevedel, Vladislav Yakovlev, and the other, anonymous, reviewer(s) for their contribution to the peer review of this work.

Reprints and permissions information is available at www.nature.com/reprints.

Publisher's note Springer Nature remains neutral with regard to jurisdictional claims in published maps and institutional affiliations.

Received: 15 July 2020; Accepted: 4 November 2020;
Published online: 15 January 2021

Related links
Key references using this protocol:
Scarcelli, G. et al. *Nat. Methods* **12**, 1132-1134 (2015): https://doi.org/10.1038/nmeth.3616
Wisniewski, E. O. et al. *Sci. Adv.* **6**, eaba6505 (2020): https://doi.org/10.1126/sciadv.aba6505
Zhang, J. et al. *Small* **16**, 1907688 (2020): https://doi.org/10.1002/smll.201907688

nature research

Corresponding author(s): Jitao Zhang and Giuliano Scarcelli

Last updated by author(s): Oct 26, 2020

Reporting Summary

Nature Research wishes to improve the reproducibility of the work that we publish. This form provides structure for consistency and transparency in reporting. For further information on Nature Research policies, see our Editorial Policies and the Editorial Policy Checklist.

Statistics

For all statistical analyses, confirm that the following items are present in the figure legend, table legend, main text, or Methods section.

n/a	Confirmed	
☒	☐	The exact sample size (*n*) for each experimental group/condition, given as a discrete number and unit of measurement
☒	☐	A statement on whether measurements were taken from distinct samples or whether the same sample was measured repeatedly
☒	☐	The statistical test(s) used AND whether they are one- or two-sided *Only common tests should be described solely by name; describe more complex techniques in the Methods section.*
☒	☐	A description of all covariates tested
☒	☐	A description of any assumptions or corrections, such as tests of normality and adjustment for multiple comparisons
☒	☐	A full description of the statistical parameters including central tendency (e.g. means) or other basic estimates (e.g. regression coefficient) AND variation (e.g. standard deviation) or associated estimates of uncertainty (e.g. confidence intervals)
☒	☐	For null hypothesis testing, the test statistic (e.g. *F*, *t*, *r*) with confidence intervals, effect sizes, degrees of freedom and *P* value noted *Give P values as exact values whenever suitable.*
☒	☐	For Bayesian analysis, information on the choice of priors and Markov chain Monte Carlo settings
☒	☐	For hierarchical and complex designs, identification of the appropriate level for tests and full reporting of outcomes
☒	☐	Estimates of effect sizes (e.g. Cohen's *d*, Pearson's *r*), indicating how they were calculated

Our web collection on statistics for biologists contains articles on many of the points above.

Software and code

Policy information about availability of computer code

Data collection	LabVIEW ver. 2016
Data analysis	MATLAB ver. R2020a

For manuscripts utilizing custom algorithms or software that are central to the research but not yet described in published literature, software must be made available to editors and reviewers. We strongly encourage code deposition in a community repository (e.g. GitHub). See the Nature Research guidelines for submitting code & software for further information.

Data

Policy information about availability of data

All manuscripts must include a data availability statement. This statement should provide the following information, where applicable:

- Accession codes, unique identifiers, or web links for publicly available datasets
- A list of figures that have associated raw data
- A description of any restrictions on data availability

The authors declare that all data supporting the findings of this study are available within the paper and its supplementary information files.

Field-specific reporting

Please select the one below that is the best fit for your research. If you are not sure, read the appropriate sections before making your selection.

☒ Life sciences ☐ Behavioural & social sciences ☐ Ecological, evolutionary & environmental sciences

For a reference copy of the document with all sections, see nature.com/documents/nr-reporting-summary-flat.pdf

Life sciences study design

All studies must disclose on these points even when the disclosure is negative.

Sample size	sample size was chosen to demonstrate the representative image acquired by the Brillouin microscope.
Data exclusions	no data were excluded from analysis.
Replication	Replication was not required in our experimental design.
Randomization	Randomization was not required in our experimental design.
Blinding	Blinding was not required in our experimental design.

Reporting for specific materials, systems and methods

We require information from authors about some types of materials, experimental systems and methods used in many studies. Here, indicate whether each material, system or method listed is relevant to your study. If you are not sure if a list item applies to your research, read the appropriate section before selecting a response.

Materials & experimental systems

n/a	Involved in the study
☒	☐ Antibodies
☐	☒ Eukaryotic cell lines
☒	☐ Palaeontology and archaeology
☒	☐ Animals and other organisms
☒	☐ Human research participants
☒	☐ Clinical data
☒	☐ Dual use research of concern

Methods

n/a	Involved in the study
☒	☐ ChIP-seq
☒	☐ Flow cytometry
☒	☐ MRI-based neuroimaging

Eukaryotic cell lines

Policy information about cell lines

Cell line source(s)	NIH 3T3 cells (ATCC Cat# CRL-6442)
Authentication	Cells were purchased directly from ATCC.
Mycoplasma contamination	Cells were not tested for mycoplasma contamination.
Commonly misidentified lines (See ICLAC register)	No commonly misidentified cell lines were used.